LUND UNIVERSITY

**Dynamic glucose enhanced chemical exchange saturation transfer MRI**

Optimization of methodology and characterization of cerebral transport kinetics

Seidemo, Anina

2023

*Citation for published version (APA):*
Seidemo, A. (2023). *Dynamic glucose enhanced chemical exchange saturation transfer MRI: Optimization of methodology and characterization of cerebral transport kinetics.* [Doctoral Thesis (compilation), Faculty of Science]. Lund University.

*Total number of authors:*
1

# Dynamic glucose enhanced chemical exchange saturation transfer MRI

## Optimization of methodology and characterization of cerebral transport kinetics

ANINA SEIDEMO
DEPARTMENT OF MEDICAL RADIATION PHYSICS
FACULTY OF SCIENCE | LUND UNIVERSITY

Dynamic glucose enhanced chemical exchange saturation transfer MRI

# Dynamic glucose enhanced chemical exchange saturation transfer MRI

## Optimization of methodology and characterization of cerebral transport kinetics

Anina Seidemo

LUND
UNIVERSITY

DOCTORAL DISSERTATION

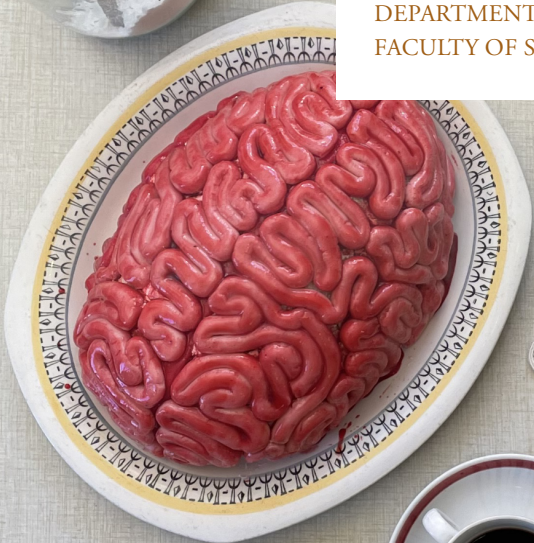| Organization<br>LUND UNIVERSITY<br>Faculty of Sciences<br>Department of Medical Radiation Physics | Document name<br>DOCTORAL DISSERTATION |
|---|---|
| | **Date of issue:** 28th April 2023 |
| Author: Anina Seidemo | Sponsoring organization |

| **Title and subtitle:** Dynamic glucose enhanced chemical exchange saturation transfer MRI<br>Optimization of methodology and characterization of cerebral transport kinetics |
|---|

**Abstract:**

Dynamic glucose enhanced (DGE) chemical exchange saturation transfer (CEST) MRI is an emerging imaging technique that provides a molecular-specific type of image contrast, based on magnetic labelling of exchangeable protons. The technique enables the use of biodegradable sugars as contrast agents, and such compounds are believed to have less side effects than conventional MRI contrast agents. However, as with most novel techniques, DGE MRI is associated with technical challenges, including small contrast enhancement compared to conventional techniques, sensitivity to motion and long scan durations. Therefore, DGE MRI is not yet ready for clinical implementation, and further evaluation and methodological development are required.

The focus of the work presented in this thesis has been on the optimization and development of DGE MRI in humans. We first implemented the DGE MRI technique at 7 T for evaluation in healthy volunteers, and subsequently optimized and applied the DGE imaging protocol at 3 T. We demonstrated that it is possible to measure arterial input functions using DGE MRI data, and that the arterial DGE MRI signal is correlated to the venous blood glucose level. Our experiments also showed that the glucose infusion duration should preferably be prolonged to minimize the sensory side effects of the injection. We also evaluated and compared DGE MRI tissue response curves in healthy tissue and in brain tumours and confirmed that DGE MRI enables differentiation of tumour from normal tissue, but that motion-related artefacts may complicate the interpretation. We developed a post-processing method for DGE MRI based on visualization of tissue response curve types with different characteristic temporal enhancement patterns. Finally, we developed a model for kinetic analysis of DGE MRI, accounting for the different signal origin and uptake kinetics of normal D-glucose.

In summary, DGE MRI has potential for tumour detection in humans and can provide information on glucose delivery, transport, and metabolism. However, further optimization of imaging and post-processing techniques is necessary, especially at lower field strengths.

| Key words |
|---|
| Classification system and/or index terms (if any) |

| Supplementary bibliographical information | **Language: English** |
|---|---|

| **ISSN** and key title | **ISBN**<br>978-91-8039-554-0 (Print)<br>978-91-8039-555-7 (PDF) |
|---|---|

| Recipient's notes | **Number of pages** | Price |
|---|---|---|
| | Security classification | |

Signature                      Date 2023-03-29

# Dynamic glucose enhanced chemical exchange saturation transfer MRI

## Optimization of methodology and characterization of cerebral transport kinetics

Anina Seidemo

*Till Pappa*

# Table of Contents

# Abstract

Dynamic glucose enhanced (DGE) chemical exchange saturation transfer (CEST) MRI is an emerging imaging technique that provides a molecular-specific type of image contrast, based on magnetic labelling of exchangeable protons. The technique enables the use of biodegradable sugars as contrast agents, and such compounds are believed to have less side effects than conventional MRI contrast agents. However, as with most novel techniques, DGE MRI is associated with technical challenges, including small contrast enhancement compared to conventional techniques, sensitivity to motion and long scan durations. Therefore, DGE MRI is not yet ready for clinical implementation, and further evaluation and methodological development are required.

The focus of the work presented in this thesis has been on the optimization and development of DGE MRI in humans. We first implemented the DGE MRI technique at 7 T for evaluation in healthy volunteers, and subsequently optimized and applied the DGE imaging protocol at 3 T. We demonstrated that it is possible to measure arterial input functions using DGE MRI data, and that the arterial DGE MRI signal is correlated to the venous blood glucose level. Our experiments also showed that the glucose infusion duration should preferably be prolonged to minimize the sensory side effects of the injection. We also evaluated and compared DGE MRI tissue response curves in healthy tissue and in brain tumours and confirmed that DGE MRI enables differentiation of tumour from normal tissue, but that motion-related artefacts may complicate the interpretation. We developed a post-processing method for DGE MRI based on visualization of tissue response curve types with different characteristic temporal enhancement patterns. Finally, we developed a model for kinetic analysis of DGE MRI, accounting for the different signal origin and uptake kinetics of normal D-glucose.

In summary, DGE MRI has potential for tumour detection in humans and can provide information on glucose delivery, transport, and metabolism. However, further optimization of imaging and post-processing techniques is necessary, especially at lower field strengths.

# Populärvetenskaplig sammanfattning

Magnetisk resonans-tomografi (MRT eller MR) är en bilddiagnostisk teknik med brett användningsområde inom den moderna sjukvården. MR-tekniken ger bilder med mycket bra mjukvävnadskontrast och har dessutom fördelen att den inte utnyttjar joniserande strålning, såsom exempelvis röntgenstrålar. För att ytterligare förbättra bildkvaliteten samt möjliggöra så kallad funktionell bildtagning, d.v.s. erhålla information om fysiologiska egenskaper, injiceras ofta ett kontrastmedel. Konventionella MR-kontrastmedel är i regel säkra men tolereras inte av vissa patientgrupper och kan även ackumuleras i vävnad efter upprepad användning. Ett kontrastmedel är ofta nödvändigt för diagnostisering av livshotande tillstånd, till exempel hjärntumörer, och därför finns det ett intresse för nya och mer skonsamma bildtagningsmetoder.

Den centrala metoden i det här avhandlingsarbetet är CEST (eng. Chemical Exchange Saturation Transfer), som är en relativt ny teknik för MR-bildtagning. Med CEST-tekniken kan en substans, till exempel socker, detekteras genom att ämnets vätekärnor märks magnetiskt (satureras) via absorption av energi från en radiofrekvent puls. Därefter sker en överföring av denna märkning från socker till vatten via en process som kallas kemiskt utbyte. Processen leder till att intensiteten i MR-bilden, som avspeglar vätekärnor i fritt vatten, ändras där ämnet är närvarande. CEST-principen kan utnyttjas så att kroppsegna eller biologiskt nedbrytbara ämnen kan användas som MR-kontrastmedel.

Om socker injiceras intravenöst samtidigt som kontinuerlig CEST-bildtagning sker, kan förändringen i varje punkt (pixel) i MR-bilden följas över tid, varvid en så kallad signalresponskurva registreras. Formen på den uppmätta signalresponskurvan kan reflektera underliggande fysiologiska egenskaper hos vävnaden, såsom exempelvis en skadad blod-hjärnbarriär. Metoden har därför potential för detektering av hjärncancer, eftersom transport över blod-hjärnbarriären och upptag av socker skiljer sig mellan tumörer och normal hjärnvävnad.

I den här doktorsavhandlingen har socker-CEST-tekniken utforskats med målet att den så småningom ska kunna implementeras för klinisk användning. Det finns fortfarande många utmaningar med tekniken, såsom att den uppmätta signalresponskurvan kan påverkas av att patienten rört sig, vilket försvårar tolkningen. Avhandlingsprojektens fokus har legat på optimering av bildtagningsparametrar och bildbehandlingsmetoder

samt utveckling av analysmodeller. Ett exempel på vad som studerades är sambandet mellan signalresponskurvan från MR-bilderna och blodsockernivåer uppmätta genom blodprov hos friska personer. CEST-tekniken applicerades även på patienter med hjärncancer, och dessa studier bekräftade att socker-CEST kan användas för att urskilja tumör från frisk hjärnvävnad. Utöver detta utvecklades en analysmetod som bygger på färgkodning av varje pixel utifrån signalresponskurvans form. Denna metod förbättrade ytterligare detektionen av tumörer och kunde dessutom ge information om sockertransport. Slutligen introducerades en matematisk modell för mer detaljerad beskrivning av sockertransport i frisk och sjuk hjärnvävnad. Sammanfattningsvis pekar resultaten på att socker-CEST har goda möjligheter för tumördetektion, men att det fortfarande finns vissa tekniska svårigheter som måste lösas innan tekniken kan introduceras i klinisk rutin. Användbarheten hos de introducerade bildbehandlingsmetoderna och analysmodellerna kan förväntas öka allteftersom CEST-bildtagningstekniken förbättras.

# Original papers

This thesis is based on three publications and one manuscript, which are referred to by their Roman numerals.

I.   Knutsson L, **Seidemo A**, Rydhög Scherman A, Markenroth Bloch K, Kalyani RR, Andersen M, Sundgren PC, Wirestam R, Helms G, van Zijl PCM, Xu X. Arterial input functions and tissue response curves in dynamic glucose enhanced (DGE) imaging: comparison between glucoCEST and blood glucose sampling in humans. *Tomography*. 2018 Dec;4(4):164-171. doi: 10.18383/j.tom.2018.00025.

II.  **Seidemo A**, Lehmann PM, Rydhög A, Wirestam R, Helms G, Zhang Y, Yadav NN, Sundgren PC, van Zijl PCM, Knutsson L. Towards robust glucose chemical exchange saturation transfer imaging in humans at 3 T: Arterial input function measurements and the effects of infusion time. *NMR in Biomedicine*. 2022 Feb;35(2):e4624. doi: 10.1002/nbm.4624.

III. **Seidemo A**, Wirestam R, Helms G, Markenroth Bloch K, Xu X, Bengzon J, Sundgren PC, van Zijl PCM, Knutsson L. Tissue response curve shape analysis of dynamic glucose enhanced (DGE) and dynamic contrast enhanced (DCE) MRI in patients with brain tumor. *NMR in Biomedicine*. 2022 Oct 30:e4863. doi: 10.1002/nbm.4863

IV.  **Seidemo A**, Lehmann PM, Yadav NN, Wirestam R, Knutsson L, van Zijl PCM. Cerebral glucose delivery, uptake and metabolism in dynamic glucose enhanced (DGE) MRI: Theory and modeling. *Manuscript*.

# List of contributions

Below is a summary of my contributions to the original papers included in this thesis:

I.  I participated in the data analysis and contributed to the interpretation of the results. I wrote parts of the first draft of the manuscript in addition to reviewing and editing all versions.

II. I took significant part in conceptualising the study. I was responsible for all data acquisition. I performed all post-processing and analysis of the data. I significantly contributed to the interpretation of the results. I was the main author of the paper.

III. I conceived the study. I developed the software for analysis and carried out all post-processing. I made significant contributions to the interpretation of the results and was the main author of the paper.

IV. I took part in conceiving the study. I significantly contributed to the theoretical model. I developed the program for the simulations and performed all analysis. I wrote the first draft of the paper together with the last author.

# Publications not included in this thesis

- Xu X, Sehgal AA, Yadav NN, Laterra J, Blair L, Blakeley J, **Seidemo A**, Coughlin JM, Pomper MG, Knutsson L, van Zijl PCM. D-glucose weighted chemical exchange saturation transfer (glucoCEST)-based dynamic glucose enhanced (DGE) MRI at 3T: early experience in healthy volunteers and brain tumor patients. *Magnetic Resonance in Medicine.* 2020;84(1):247-262. doi: 10.1002/mrm.28124

- Lehmann PM, **Seidemo A**, Andersen M, Xu X, Li X, Yadav N, Wirestam R, Liebig P, Testud F, Sundgren PC, van Zijl PCM, Knutsson L. A numerical human brain phantom for dynamic glucose-enhanced (DGE) MRI: On the influence of head motion at 3 T. *Magnetic Resonance in Medicine.* 2023 May;89(5):1871-1887. doi: 10.1002/mrm.29563

# Abbreviations and symbols

| | |
|---|---|
| 2-DG | 2-deoxy-D-glucose |
| 2-DG-6P | 2-deoxyglucose-6-phosphate |
| 3-OMG | 3-O-methyl-D-glucose |
| AIF | Arterial input function |
| APT | Amide proton transfer |
| ATP | Adenosine triphosphate |
| AUC | Area under curve |
| $B_1$ | RF saturation field strength |
| BBB | Blood-brain barrier |
| $C_c$ | Intracellular concentration |
| $C_e$ | Extravascular extracellular space concentration |
| $C_m$ | Phosphorylated glucose concentration |
| $C_p$ | Plasma concentration |
| CESL | Chemical exchange-sensitive spin lock |
| CEST | Chemical exchange saturation transfer |
| $CMR_{glc}$ | Cerebral metabolic rate of glucose |
| CSF | Cerebrospinal fluid |
| DCE | Dynamic contrast enhanced |
| DGE | Dynamic glucose enhanced |
| E | Enzyme |
| EES | Extravascular extracellular space |
| EM | Electromagnetic |
| ES | Enzyme-substrate complex |
| $f_b$ | Compartmental fraction of blood |
| $f_e$ | Compartmental fraction of EES |
| FDG | Fluorodeoxyglucose |
| G-6P | Glucose-6-phosphate |
| GEF | Glucose extraction fraction |
| glucoCESL | glucose CESL |

| | |
|---|---|
| glucoCEST | glucose CEST |
| GLUT1 | Glucose transporter 1 |
| GLUT3 | Glucose transporter 3 |
| GLUT5 | Glucose transporter 5 |
| GM | Grey matter |
| HK | Hexokinase |
| i.v. | Intravenous |
| $J$ | Flux (transport rate) |
| $K_{ep}$ | Wash-out constant unit |
| $k_{ex}$ | Chemical exchange rate |
| $K_M$ | Michaelis-Menten half-saturation constant for enzyme |
| $K_T$ | Half-saturation constant for transport |
| $K^{trans}$ | Volume transfer constant |
| MM | Michaelis-Menten |
| MRS | Magnetic resonance spectroscopy |
| MT | Magnetization transfer |
| $MTR_{asym}$ | Magnetization transfer ratio asymmetry |
| MTC | Magnetization transfer contrast |
| MTR | Magnetization transfer ratio |
| NOE | Nuclear Overhauser enhancement |
| OH | Hydroxyl |
| P | Product |
| PET | Positron emission tomography |
| PTR | Proton transfer ratio |
| PVE | Partial volume effect |
| RF | Radiofrequency |
| ROI | Region of interest |
| S | Substrate |
| $S_{base}$ | Average baseline signal |
| $S_{in}$ | Wash-in slope |
| $S_{max}$ | Maximum enhancement |
| $S_{out}$ | Wash-out slope |
| SAR | Specific absorption rate |
| SGLT | Sodium-glucose linked transporter |
| $t_d$ | Inter-pulse delay |

| | |
|---|---|
| $T_{max}$ | Maximum transport rate |
| $t_p$ | Pulse duration |
| $T_{sat}$ | Duration of saturation period |
| TCA | Tricarboxylic acid |
| TIC | Time-intensity curve |
| TSE | Turbo spin echo |
| TTP | Time-to-peak |
| $V_{max}$ | Maximum possible rate |
| WASSR | Water saturation shift referencing |
| WM | White matter |
| $x_s$ | Fraction of solute protons with respect to water protons |
| $\alpha$ | Saturation efficiency |
| $\Delta\omega$ | Chemical shift difference between solute proton pool and water proton pool, also referred to as saturation frequency offset in Z-spectra |

# 1. Introduction and aims

Diagnosis of brain cancer is commonly accomplished by medical imaging modalities such as computed tomography (CT), magnetic resonance imaging (MRI) and positron emission tomography (PET). Tracers or contrast agents are often administered either to enable imaging or to improve the specificity and sensitivity of relevant morphological or functional image features. These substances can be radioactive (in PET), iodinated (in CT) or metallo-ionic complexed (in MRI). One example of functional imaging is perfusion MRI in the brain, where a gadolinium-based contrast agent is administered intravenously followed by dynamic MR image acquisition. Using model-based analysis of tracer kinetics, information about blood flow (perfusion), blood volume and blood-brain barrier (BBB) permeability can be retrieved from the signal change over time, caused by the passage of the contrast agent. Such a temporal signal change is often referred to as a tissue response curve, and its characteristics depends on the specific contrast agent and method of imaging. The gadolinium-based contrast agents for MRI used today are considered safe but have been linked to the rare disease nephrogenic systemic fibrosis (1, 2) in patients with renal impairment. Additionally, gadolinium can accumulate in brain tissue (3-6) and bone (7) after repeated use. Furthermore, the diagnostic usefulness of conventional MRI contrast agent methods is restricted by the fact that not all tumours are contrast-enhancing (8). Also, the methods show limited ability to distinguish between low and high grade tumours (8, 9) and, most importantly, to distinguish true progression from pseudo-progression after treatment (10-13). Concerns regarding gadolinium have also been raised from an environmental point of view (14), as there is evidence of gadolinium pollution in water close to large imaging facilities (15). Hence, the implementation of new types of contrast agents and methods is desirable.

Chemical exchange saturation transfer (CEST) MRI (16) is an emerging technique that can provide physiological information without the use of ionizing radiation or potentially toxic substances. The method exploits the naturally occurring chemical exchange of protons between molecules and enables the use of endogenous and/or biodegradable compounds as contrast agents. For instance, hydroxyl protons in natural sugar, D-glucose, can be labelled by a radiofrequency (RF) pulse, and the labelled protons are subsequently transferred to water, causing a measurable signal change in the images. D-glucose can thus act as a biocompatible CEST contrast agent to facilitate an approach named glucoCEST (17, 18). During the last ten years, MRI studies using

glucoCEST or chemical exchange-sensitive spin-lock using D-glucose (glucoCESL (19)) have shown that information about microvasculature, BBB permeability and D-glucose uptake in tumours can be obtained (17, 20-24). GlucoCEST provides a molecule-specific MRI contrast and has preclinically shown potential to differentiate between tumour phenotypes (17, 18). In humans, dynamic glucoCEST or glucoCESL (dynamic glucose-enhanced, DGE) MRI has been applied to brain tumour patients (20, 22, 24-26) and to human placenta (27). GlucoCEST has also been used in patients with head and neck cancer (28) and in preclinical Alzheimer's disease models (29-31). Besides being safer than conventional contrast agents, and thus more suitable for application in sensitive patient groups such as children or patients with renal impairment, glucoCEST has potential for early detection of disease. In addition to its biodegradability, the advantages of D-glucose as an MRI contrast agent include low cost and high accessibility.

The challenges in DGE MRI include small effect size, especially at clinical magnetic field strengths (25), and long scan durations. This makes DGE MRI vulnerable to patient motion, which can produce signal changes of the same order of magnitude as the true CEST signal (32). Furthermore, the mechanism and compartmental origin of the glucoCEST contrast in the human brain images is not yet fully understood, complicating the interpretation of DGE MRI tissue response curves. In the research conducted for completion of this thesis, some of these challenges were addressed.

In resemblance to gadolinium-based perfusion MRI, dynamic tissue response curves are also measured in DGE MRI. Such curves can provide information on the underlying physiology, for example by estimation of perfusion-related parameters. The acquisition, extraction, characterization, and interpretation of dynamic response curves can be considered as one of the central topics of this thesis. In summary, the work proceeds through increasingly advanced levels of analysis of DGE MRI tissue response curves. Papers I and II focus on visual analysis of images and DGE MRI tissue response curves. In Paper III, a deeper analysis of response curve shapes was performed, and in Paper IV the complexity was increased further by utilizing kinetic modelling.

The aim of the study in Paper I, was to implement DGE MRI in healthy volunteers at 7 T, to investigate the feasibility of measuring arterial input functions (AIFs), and to compare the AIFs to the time dependent changes in venous blood glucose level to examine the relationship between DGE MRI signal and blood glucose concentration. The objective of Paper II was to take a step towards clinical implementation by performing DGE MRI in healthy volunteers at 3 T, and to optimize the glucoCEST scanning protocol at 3 T. An additional aim was to investigate the choice of glucose infusion rate. In Paper III, the aim was to develop a data analysis approach based on tissue response curve shapes, and to analyze the results in terms of spatial as well as temporal differences and similarities between D-glucose and gadolinium enhancement in brain tumours. Finally, in Paper IV, the knowledge gained from the previous work

(Paper I – Paper III), and from MR spectroscopy (MRS) and nuclear medicine literature, was used to develop, validate, and apply a kinetic modelling method for DGE MRI, with the goal to gain insight into the compartmental origin of the DGE MRI signal and to obtain more detailed physiological information.

The general aim of this thesis was to develop and apply the glucoCEST MRI method in healthy volunteers and brain tumour patients in order to evaluate its potential for combined imaging of perfusion, BBB permeability and cellular uptake in tumours.

# 2. Chemical exchange saturation transfer MRI

Chemical exchange saturation transfer magnetic resonance imaging is a long name that may seem intimidating at first glance, especially if you are not an MR physicist. To prevent you from stop reading immediately, we will start by breaking this grotesquely long name into pieces to try to understand what is actually in there.

*Chemical exchange* is a process in which atoms or molecular groups move physically between different molecular environments. For instance, weakly bound protons in different molecules can switch places with each other.

To understand what *saturation* means, we first need to understand a bit more about *magnetic resonance imaging*. The theory and principles behind MRI will not be discussed in detail in this thesis. For the sake of space, only a very simplified and brief explanation will be provided: In MRI, we are usually detecting the signal from hydrogen nuclei, protons, in water. When placed in an external static magnetic field with magnetic flux density ($B_0$), the protons create a net magnetization vector that is parallel to the direction of $B_0$. In addition, the proton magnetic dipoles will perform a circular motion, precession, similar to a gyroscope, around the direction of $B_0$. The precession frequency, also referred to as the resonance frequency, depends on the strength of $B_0$ and is also specific for a given nuclide as determined by its gyromagnetic ratio ($\gamma$). The measured signal, which is used to form the MR image, is proportional to the net magnetization vector. However, the net magnetization is not detectable when aligned with the much larger $B_0$, why the first step in creating an image is to tip the net magnetization vector away from the $B_0$ direction towards the transverse plane (perpendicular to $B_0$) where it can be distinguished from $B_0$. This is called excitation and can be achieved by applying an alternating electromagnetic (EM) field with a frequency that matches the resonance frequency. For hydrogen nuclei, the resonance frequency is in the RF range and the short-lived EM field used for excitation is therefore referred to as an RF pulse.

Saturation is a general term used when the detectable signal is reduced, due to a reduced magnitude of the net magnetization vector, which can for instance be accomplished with long RF irradiation (of the order of $T_1$ or longer). Due to microscopic differences in the magnetic environment caused by variabilities in electron shielding, protons will

experience slightly different resonance frequencies. In this manner, certain proton pools can be selectively saturated, and, at the subsequent excitation, there will be no residual parallel net magnetization to tip down to the transverse plane when creating the image. The measured signal from saturated proton pools will thus be negligible.

The word *transfer* refers to the transfer of magnetization, or as in the case of CEST, more specifically transfer of saturation. If one proton pool (magnetic environment) is saturated, and if the protons in this pool are exchangeable (weakly bound), the chemical exchange process will result in protons moving from this pool to another pool. The saturation will thus be transferred from the first pool to the second. In CEST, the first pool represents protons in a compound present in small concentration in solution. The second pool is the much larger water pool (solvent), which is used to generate the signal that forms the MR image.

Putting all the words back together, chemical exchange saturation transfer MRI is an imaging approach in which a proton pool in a molecule of interest is labelled (saturated), after which these protons spontaneously switch places with protons in water (a process called chemical exchange), resulting in a transfer of saturation to the water signal. This process repeats itself during the RF irradiation, thereby increasing the saturation of the water pool. A signal reduction can then be measured in the MR image in regions where the molecule of interest is present. This process allows for detection of molecules present in low concentrations, which cannot be detected directly using excitation or saturation. Throughout this chapter, the principles and contrast mechanisms behind CEST are discussed, and a brief overview of CEST MRI applications is given.

## 2.1  Magnetization transfer

The term magnetization transfer (MT) includes chemical exchange, as well as other processes that are important for understanding and interpreting CEST MRI.

Magnetic dipoles, such as hydrogen protons in water, can interact through so-called dipolar coupling. The strength of this coupling depends on the relative orientation and distance between the protons. Magnetization can be transferred between neighbouring protons that interact through dipolar coupling; a process called cross-relaxation. Saturation can thus be transferred not only between molecules, but also between protons within molecules, since one spin pool can affect an adjacent coupled spin pool through cross-relaxation. This is different from chemical exchange in that only saturation is transferred, while the protons themselves keep their positions. The cross-relaxation effect increases with decreasing molecular motion and is therefore more effective in semi-solids than in aqueous tissues. Nuclear Overhauser enhancement

(NOE) is such an effect, where cross-relaxation due to dipolar coupling causes polarisation or saturation to spread through a molecule. This process is also sometimes called spin diffusion.

Saturation can be transferred intra- or intermolecularly by pure cross-relaxation, or through a combination of NOE and exchange, so called relayed NOE (rNOE), and can take many forms. Exchange-relayed NOE represents a process where saturation is transferred to a macromolecule via proton chemical exchange from a water molecule, followed by spin diffusion relaying the saturation throughout the molecule. In the reverse process, NOE-relayed exchange, a proton pool in a macromolecule is saturated, whereafter the saturation spread through the molecule by cross-relaxation before finally being transferred to a hydrogen proton in water via chemical exchange.

Semi-solid macromolecules with reduced mobility, for example, in membranes or myelin, exhibit strong dipolar intramolecular coupling (with coupling constants in the order of 10 kHz) and have short $T_2$ (microsecond range). Because of the dipolar coupling, these molecules give rise to resonances over a broad frequency range, allowing for saturation of the semi-solid proton pool by an RF pulse applied at a frequency outside the proton spectral range of solutes in liquids (1-10 ppm in MRS, or ±5 ppm around the water frequency). Such far off-resonance (different from the water resonance frequency) saturation leaves mobile molecules unaffected, but saturation will be transferred to the water pool through the processes described above. Similarly, excitation of this far off-resonance component will lead to fast signal decay (due to the short $T_2$), which is another type of signal saturation. Both selective irradiation and pulsed saturation can be used to create images with magnetization transfer contrast (MTC) caused by dipolar interactions between water protons and protons in solid-like macromolecules. MTC dominates in semi-solid tissues, while CEST dominates for mobile molecules.

## 2.2 CEST principles and contrast mechanisms

As already stated, the standard MRI signal is based on water. Due to variations in the local molecular magnetic environment, protons in a target molecule other than water, for example D-glucose, show a slightly different resonance frequency than the hydrogen protons in water, allowing for selective RF saturation. In CEST MRI, this particular frequency difference is often expressed as the chemical shift difference ($\Delta\omega$) in parts per million (ppm) relative to the water resonance frequency. In this manner of referencing, the chemical shift difference of a certain exchangeable proton pool will be the same, for example, 2 ppm, regardless of field strength. The target compound, often referred to as the solute, is present in low concentrations in vivo (μM or mM) compared to water

(111 M), and his makes direct detection of the solute difficult. However, if the solute protons are exchangeable, the saturation can be transferred to water via chemical exchange (33), producing a modest reduction of the water signal (16, 34). In the exchange process, protons from the saturated solute pool are continuously being replaced by protons from the unsaturated water pool. While the RF irradiation is on, this ongoing chemical exchange process and the resulting continuous transfer of saturation will lead to a build-up of saturation in water and ultimately a measurable signal attenuation in the MR image. The degree of saturation of the water signal as a function of saturation frequency offset from water frequency is referred to as a Z-spectrum (35). The chemical exchange saturation transfer process and a Z-spectrum are schematically illustrated in Figure 2.1. Note the convention based on MR spectroscopy that the higher frequency is to the left. Contrary to MRS, the frequency scale in the Z-spectrum is referenced to the central water frequency, in CEST assigned the value 0 ppm (4.75 ppm in MRS). Thus, positive saturation frequency offsets are placed to the left and negative offsets are placed to the right of the water frequency.
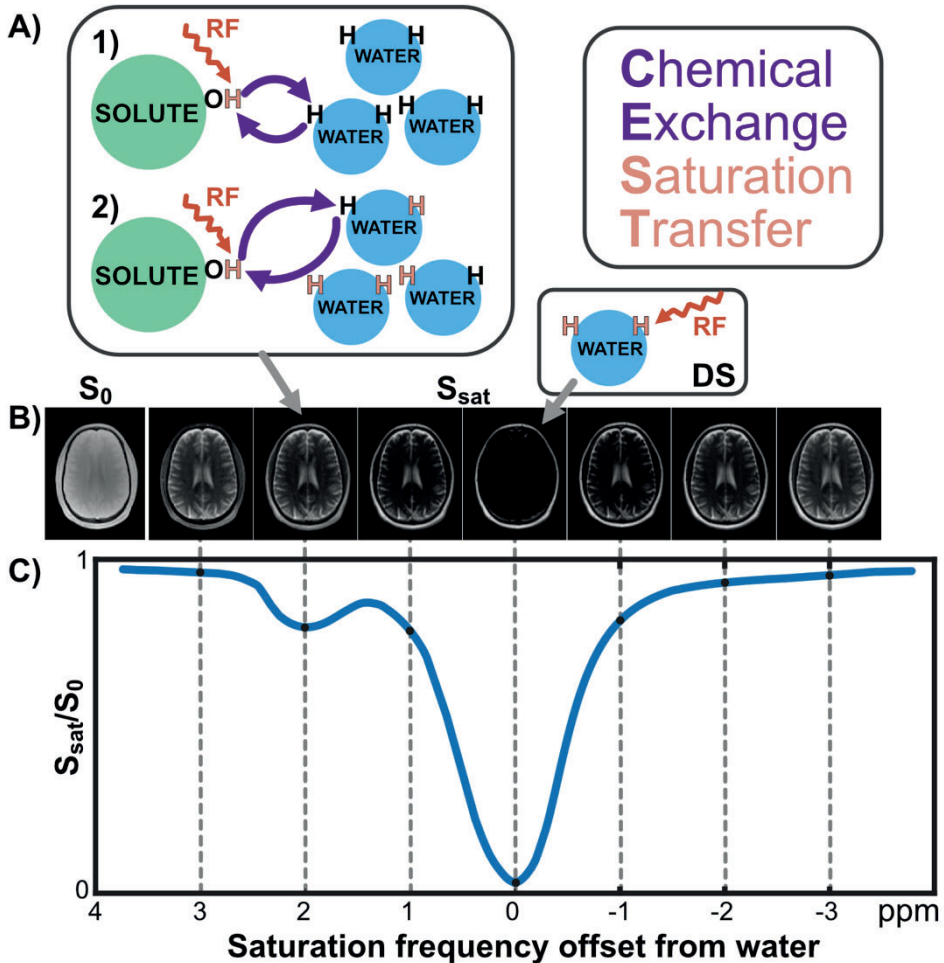
**Figure 2.1**. Illustration of the saturation of hydroxyl (-OH) protons in a fictional target molecule (solute), chemical exchange between -OH and water (solvent), and the subsequent effect on the water signal (the Z-spectrum). A) After saturation of the -OH protons in the solute, the saturation is transferred to water through chemical exchange. This process is repeated and leads ultimately to a decrease in the water signal in regions where the solute is present. B) The $S_{sat}$ images are collected after saturation at different frequency offsets from the water frequency, and the varying intensity in the images is a consequence of saturation transfer. The $S_0$ image represents the reference signal intensity without saturation and the 0 ppm image reflects direct saturation (DS) of water. C) A Z-spectrum can be calculated for each voxel by normalizing each saturated image intensity $S_{sat}$ to the non-saturated image intensity $S_0$. The CEST effect causes a small dip seen at the resonance frequency of the solute, in this case at a frequency offset of around 2 ppm. A large dip is seen at the water resonance frequency (0 ppm), due to DS effects.

The CEST effect depends on solute concentration, solute proton exchange rate, RF magnetic field strength ($B_1$), saturation duration and longitudinal relaxation time of water (25, 36, 37). The CEST mechanism can be described theoretically by the Bloch-McConnell equations (38). These equations modify the standard Bloch equations by incorporating magnetization transfer processes between two spin pools. As described by, for example, van Zijl and Sehgal (39) the analytical solution to the Bloch-McConnell equations can under the assumption of slow exchange on the NMR time scale, no back-exchange of saturated protons, and no direct saturation of water, be simplified to Eq. 2.1a. This equation designates the proton transfer ratio (PTR), which can be derived from the ratio of the saturated signal $S_{sat}$ and the non-saturated reference signal $S_0$, representing the CEST effect.

$$\text{PTR} = \frac{S_{sat}}{S_0} = x_{\text{s}} \cdot \alpha \cdot k_{\text{ex}} \cdot T_{1\text{w}} \cdot \left(1 - e^{-T_{\text{sat}}/T_{1\text{w}}}\right). \qquad \text{(Eq. 2.1a)}$$

Here, $x_{\text{s}} = \frac{[\text{exchangeable protons}]}{[\text{water protons}]}$ (the concentration of solute protons relative to water protons), $\alpha$ is the saturation efficiency as described by Eq. 2.1b, $k_{\text{ex}}$ is the proton exchange rate from solute to water, $T_{1\text{w}}$ is the longitudinal relaxation time of water and $T_{\text{sat}}$ is the saturation duration. The saturation efficiency, $\alpha$, depends mainly on $B_1$ and $k_{\text{ex}}$, and can be approximated by:

$$\alpha \approx \frac{(\gamma B_1)^2}{(\gamma B_1)^2 + (k_{ex})^2}. \qquad \text{(Eq. 2.1b)}$$

$\alpha = 1$ for a fully saturated proton pool, and $\alpha = 0$ for a totally unsaturated proton pool.

For successful CEST detection, the exchange rate should be in the slow ($k_{ex} \ll \Delta\omega$) to intermediate ($k_{ex} \approx \Delta\omega$) range on the NMR time scale (16). The chemical shift difference with water must be large enough for the solute protons to be selectively saturated, thereby minimizing direct saturation of water. As seen in Eq. 2.1a, the CEST effect increases with the exchange rate. However, the exchange rate should not be too high as the solute protons must be given time to become sufficiently saturated before they exchange. In summary, the optimal exchange regime for selective saturation is when the chemical shift difference between the proton pool frequency and the water proton pool frequency is equal to or greater than the exchange rate (16, 39),

$$\Delta\omega \geq k_{ex}, \qquad \text{(Eq. 2.2)}$$

where $\Delta\omega$ is the chemical shift offset, i.e. the difference in resonance angular frequency between solute and water in radians/second and $k_{ex}$ is the chemical exchange rate in s$^{-1}$. If the exchange rate is fast compared to the chemical shift, the frequency specificity

will be lost (signal coalescence), and separation of the individual solute resonances from water will not be possible. Too slow an exchange would mean that very few exchanges occur, and thus no detectable CEST effect. Numerical examples of exchange rates and chemical shifts for hydroxyl protons in glucose at different $B_0$ are shown in Chapter 4.1.1.

To understand the coalescence of the solute and water resonances, consider an NMR spectrum of two exchanging proton pools at two different resonance frequencies. If the exchange is slow, the separate resonances (peaks) for the two pools are visible. When the exchange rate increases, so does the line width of the peaks. As the exchange rate increases to the intermediate regime, the peaks of the exchanging pools start to coalesce. At fast exchange rates, the two peaks will merge into one single peak centred at the average resonance frequency of the two peaks, and this peak will narrow as the exchange rate increases (the averaged value is getting more precise).

The CEST effect strongly depends on magnetic field strength, which can be understood from Eqns. 2.1a and 2.2. The separation between the solute and water resonances increases with field strength, and such an increase in spectral resolution reduces the contribution from direct water saturation (37, 40). A larger chemical shift difference allows for detection of compounds with faster exchange rates, which is also beneficial for the CEST effect. Moreover, the longer $T_1$ at higher magnetic fields (41, 42) allows the saturation to remain for a longer period of time (39).

The CEST effect also depends on temperature and pH. Peak coalescence increases with increased temperature, because the faster movement of the molecules leads to an averaged resonance frequency instead of separate peaks. The pH dependence of the exchange rate is rather complicated but depends on electrostatic field effects affecting the ionic binding (43) and the presence of catalysts, which in turn affect the probability of exchange. A change in pH may accelerate or inhibit proton exchange, depending on whether the exchange is base, acid or buffer catalysed. The exchange rates of protons in a solution can be described as the sum of the effects of acid catalysed exchange, base catalysed exchange, buffer-catalysed exchange, and other possible contributions (44).

An in vivo Z-spectrum includes contributions from direct water saturation as well as several types of MT (CEST, NOE and MTC), depending on $B_1$ and magnetic field strength $B_0$, but also on the tissue constituents because of the differences in molecular motion and interactions between, for example, immobile macromolecules and free water. The shape of the Z-spectrum can therefore provide information about the tissue environment. Altered tissue properties, in, for example, ischaemia or tumours, affect the type of MT, and therefore also the Z-spectrum and the PTR (45, 46).

The semisolid saturation transfer effects (MTC) are often assumed to be symmetric around the water frequency, an assumption that might not always be true (37). MTC creates a broad background throughout the entire Z-spectrum and is slightly

asymmetric, especially in white matter due to the average resonance frequency of myelin aliphatic protons (47). The relative contributions of CEST, NOE and MTC change with $B_1$, with the MTC increasing more strongly. Hence, it is complicated to determine the relative contribution of each MT process in a given Z-spectrum. The direct water saturation line shape can be assumed to be symmetric around the water resonance frequency, and the DS contribution can thus be removed by performing magnetization transfer ratio asymmetry ($MTR_{asym}$) analysis, as described in Eq. 2.3.

$$MTR_{asym} = MTR(\Delta\omega) - MTR(-\Delta\omega) = \qquad \text{(Eq. 2.3)}$$

$$\frac{S_0 - S_{sat}(\Delta\omega)}{S_0} - \frac{S_0 - S_{sat}(-\Delta\omega)}{S_0} = \frac{S_{sat}(-\Delta\omega) - S_{sat}(\Delta\omega)}{S_0},$$

where $S_{sat}(\Delta\omega)$ is the signal at one positive saturation frequency offset, $S_{sat}(-\Delta\omega)$ is the signal at the corresponding negative frequency offset, and $S_0$ is the signal without saturation. $MTR_{asym}$ analysis does not isolate the CEST effect entirely, because all asymmetric effects will contribute, such as for example rNOEs from aliphatic protons on the negative side in the Z-spectrum.

In summary, CEST MRI can provide molecule-specific image contrast based on saturation transfer between molecules having proton pools with different resonance frequencies. This makes CEST comparable to MRS, but CEST has higher sensitivity because of indirect detection through the much larger water pool. However, CEST is less specific than MRS, because of the much broader resonances of the exchanging protons.

## 2.3  CEST imaging

A CEST MRI pulse sequence consists of two main blocks: saturation (RF preparation) and image acquisition. In the saturation part, a series of RF pulses or continuous wave RF irradiation is applied at one or multiple frequency offsets relative to water, with the total duration $T_{sat}$ often being of the order of seconds. In the pulsed approach, each RF pulse has a duration $t_p$ and is separated by an inter-pulse delay $t_d$, thereby together resulting in a total saturation duration $T_{sat}$. As seen in Eq. 2.1a, the CEST effect increases with $T_{sat}$. Increased RF field strength, $B_1$, increases the CEST effect as well as the MTC contribution, as illustrated by the simulated Z-spectra as a function of $B_1$ in Figure 2.2. In vivo, $B_1$ is limited by RF hardware and by specific absorption rate (SAR) restrictions. Therefore, pulsed saturation is often chosen over a continuous wave approach.
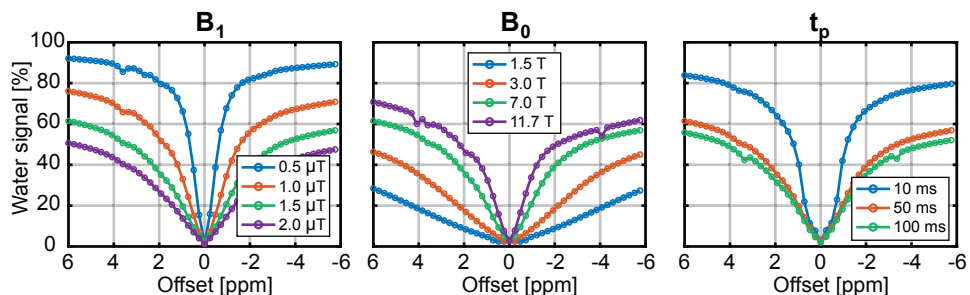
**Figure 2.2**. Simulated Z-spectra in grey matter for pulsed saturation showing the dependence of $B_1$ (left), $B_0$ (centre), and $t_p$ (right). When not varied, the following parameters were used: $B_1$ = 1.5 µT, $B_0$ = 7 T, $t_p$ = 50 ms, $t_d$ = 25 ms, 32 sinc-gauss pulses. The simulations were performed using the Bloch-McConnell equations as described by Xu et al. (25). The parameters used in the simulation are summarized in Paper IV.

In a CEST experiment, several saturation parameters need to be optimized, depending on application and field strength. As an example, solutes with fast exchange rates require higher saturation strength $B_1$ for effective saturation (48), also seen in Eq. 2.1b. The saturation parameters used in Papers I – III are shown in Table 2.1, and serve as an example of the typical order of magnitude for these parameters. CEST protocol optimization and the choice of saturation parameters are also discussed in Chapter 6.

**Table 2.1**. Saturation parameters used in Papers I-III.

| | $B_0$ [T] | $B_1$ [µT] | $t_p$ [ms] | $t_d$ [ms] | No. of pulses | $T_{sat}$ [s] | Pulse shape |
|---|---|---|---|---|---|---|---|
| **Papers I & III** | 7 | 1.96 | 50 | 25 | 32 | 1.6 | Sinc-gauss |
| **Paper II** | 3 | 0.6 | 100 | 10 | 10 | 1 | Gauss |
| | | 1.6 | | | | | |

The image acquisition part is performed after the saturation block using fast acquisition techniques, such as turbo spin echo (TSE), used in Paper II, gradient echo (GRE), used in Papers I & III, or echo-planar imaging (EPI) (49). Different sorts of acceleration approaches and undersampling techniques have been proposed in CEST imaging (49-56). However, a detailed description of such techniques is beyond the scope of this thesis.

## 2.4 CEST applications in the brain

CEST MRI was first demonstrated by Ward et al. in 2000, and the exchange rates and chemical shifts of a number of compounds were evaluated under physiological pH and temperature conditions to determine their suitability as exogenous contrast agents for CEST MRI (16). In theory, almost any compound including a chemical group with exchangeable hydrogen protons is suitable for CEST imaging. The ideal CEST contrast agent has a large chemical shift difference and obeys Eq. 2.2. For imaging in humans, it should preferably be an endogenous or non-toxic exogenous substance. Suitable proton groups in such compounds are hydroxyl (-OH), amide (-NH) and amine (-$NH_2$), showing chemical shifts of the order of 0-3.5, 3.5 and 2-3 ppm relative to water, respectively (36). Although many potential CEST contrast agents exist, development of exogenous agents has mainly been focused on drugs in clinical use or agents already approved for other imaging methods (57).

The first brain tumour CEST method based on an endogenous compound was introduced in 2003 by Zhou et al. (45), who showed that mobile proteins in millimolar concentrations could be detected in rat glioma. This technique called amide proton transfer-weighted (APTw) MRI was also the first technique to make it into the clinic, as it recently became an FDA-approved product (58). APTw MRI has been studied extensively during the last two decades, and the applications include detection and grading of brain tumours (59-66), genetic marker identification (67-70), separation of treatment effect (e.g. radiation necrosis) from tumour recurrence (71-74), as well as prognostic estimation of tumour progression and survival (75, 76). APTw MRI has also been used for imaging of ischemic stroke because of the reduced pH in ischemic regions, causing a reduction in the proton exchange rate, which in turn leads to a lower APTw signal (46, 77, 78). APTw MRI has a strength in that it is completely non-invasive since it relies on endogenous effects such as increased protein concentrations in tumours. As discussed in the previous two sections, the CEST contrast depends strongly on the RF parameters used, which will lead to varying relative contributions of saturation transfer effects in the Z-spectrum. This is the reason for the 'w' in APTw MRI – the detected signal is merely APT-weighted.

Exogenous compounds have included different sorts of sugars (57). These are administered intravenously as biodegradable contrast agents for tumour visualization and to obtain information about glucose delivery, transport, and metabolism. This technique, dubbed glucoCEST, is the focus of this thesis and is therefore described in further detail in the following chapters.

# 3. Glucose in the brain

The CEST MRI method has now been introduced, together with its potential and challenges. Throughout the next few chapters, the how's and why's of using glucose as a CEST contrast agent will be discussed, but first a short introduction to glucose physiology in the normal and diseased brain will be given.

The human brain is fuelled primarily by D-glucose and a continuous and well-regulated supply is essential for normal function. An adult human brain consumes approximately 5.6 mg D-glucose per 100 g brain tissue per minute (79). This means that the brain of a healthy adult consumes around 100 g of D-glucose per day. In this chapter, we will follow the journey of D-glucose from blood to brain, until it meets its final destiny within the cells, where it is metabolized. The administration of D-glucose, i.e. how it gets into the blood stream, will not be discussed. However, the path and fate of glucose will be the same, regardless of whether it is ingested or injected intravenously. The delivery of glucose to the brain tissue is driven by the lower concentration of D-glucose in the brain relative to blood. This concentration difference is maintained by the continuous metabolism of D-glucose within the brain cells.

Hypoglycaemia is defined as blood D-glucose levels below 3.9 mM (70 mg/dL), while the normal fasting blood D-glucose levels (normo- or euglycemia) are between 3.9 and 6.1 mM (110 mg/dL) (80). Hyperglycaemia (> 6.1 mM) leads to increased insulin secretion, and subsequently to increased D-glucose uptake in muscles and in the liver, which leads to lower blood D-glucose level. The arterial D-glucose concentration is higher than the venous, and the D-glucose extraction fraction (GEF) in the brain is around 0.11 (81-83).

The brain and the central nervous system are protected from potentially harmful substances by the BBB, which carefully regulates the transport of substances between blood and brain. The BBB consists of the two endothelial membranes situated on each side of the endothelial cell layer which line the brain capillaries. A simplified illustration of the BBB and a brain capillary is shown in Figure 3.1.

## 3.1 Cerebral D-glucose transport and metabolism

Glucose circulates in the blood and reaches the brain extravascular extracellular space (EES) via transporter proteins, primarily glucose transporter 1 (GLUT1) in the endothelial cells of the BBB, meaning that glucose does not diffuse freely from blood to brain, and the transport can become saturated. The transport between blood and brain is bidirectional, and GLUT1 is asymmetrically distributed between the luminal (blood-facing) and abluminal (brain-facing) membranes of the BBB (84), with a higher abundance in the abluminal membrane (85, 86), as indicated in Figure 3.1. The ratio of GLUT1 on the abluminal and luminal sides has been hypothesized to change during various physiological conditions, leading to changes in the glucose transport rate over the BBB (84).
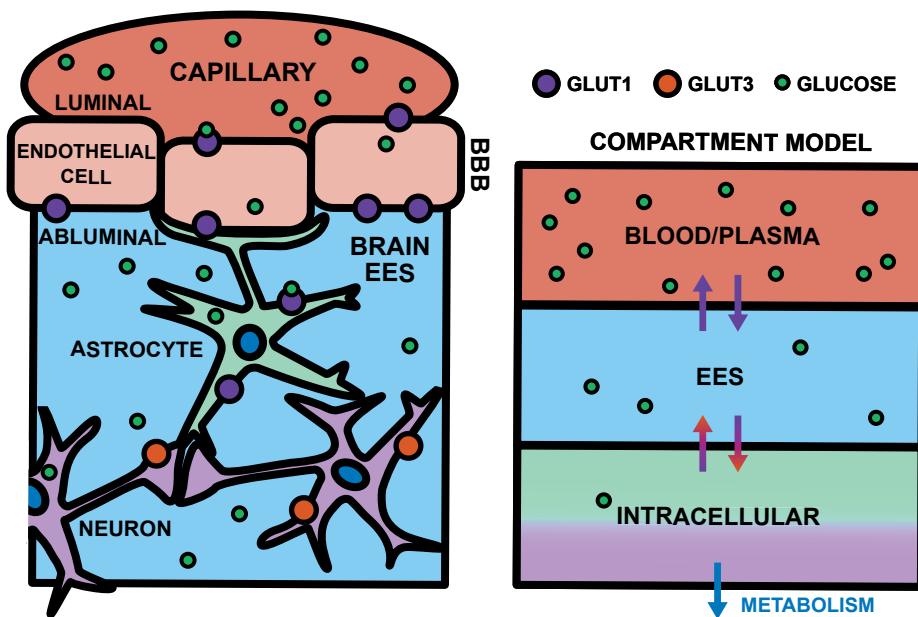


**Figure 3.1**. Left: Simplified illustration showing the blood brain barrier (BBB), the location of different glucose transporters (GLUTs) in the brain, and the transport of glucose from blood to brain extravascular extracellular (EES) space and into brain cells. Glucose can either be transported directly from the BBB into astrocytes, or over the BBB into brain cells via the EES. For the purpose of describing the relative glucose concentration, or for modelling, the neurovascular unit is often simplified. The figure to the left can then be simplified by a three-compartment model, shown to the right.

The cerebral influx rate of glucose depends on the concentration gradient between blood and brain (79), meaning that the GLUT-mediated transport tends towards concentration equilibrium, and the net flux of glucose over a membrane is zero in the absence of a concentration gradient (87). The glucose transport over the BBB and into the brain is increased by neural activation (88, 89), in response to the increased energy consumption. At rest, however, cerebral metabolism can be regarded as constant. Throughout this thesis, only the resting brain (i.e. baseline activity) will be considered, which is a valid assumption for the experimental conditions.

After crossing the BBB into the EES, glucose is further transported into the different types of brain cells, where it is metabolized. As shown in Figure 3.1, glucose enters astrocytes/glial cells via GLUT1 transporters, and neurons by GLUT3 transporters. GLUT1 and GLUT3 are the predominant glucose transporters in the brain (84, 85, 90), but other GLUTs, such as GLUT5 which is the major transporter in microglia, partake in glucose transport throughout the neurovascular system. GLUTs are sodium-independent transporters, and in addition to these there are also sodium-dependent transporter proteins, referred to as sodium-glucose linked transporters (SGLT). These can transport glucose against the concentration gradient, because the driving force is the flux of sodium which is directed opposite to the flux of glucose (85). However, the presence of SGLTs has not been established in the brain (85). For our purposes, it is therefore enough to consider only the major transporters in BBB and astrocytes (GLUT1) as well as in neurons (GLUT3).

Inside the cell, the first step of the glycolysis (the metabolic pathway of glucose) is the conversion from glucose to glucose-6-phosphate (G-6P), catalysed by the enzyme hexokinase I (HK). G-6P cannot exit the cell and more glucose will be drawn into the cell to preserve the concentration ratio. This first irreversible step of the glycolysis is the rate-limiting step but also the driving force in cerebral glucose transport. Hexokinase actions are saturated at brain glucose levels >1 mM, so the rate of glucose metabolism is maximal and independent of the plasma glucose concentration under normal conditions. The glucose utilization, or cerebral metabolic rate of glucose ($CMR_{glc}$), in the healthy adult resting brain is around 0.3 μmol/g/min (81, 91-95). The combination of stable transport over BBB and the constant metabolism ensures that brain glucose availability always satisfies the energy demand/glucose requirements. The end product of glycolysis is pyruvate, and in normal cells, most of the pyruvate is converted into acetyl-CoA. Finally, 36 adenosine triphosphate (ATP) per glucose are produced by the tricarboxylic acid (TCA) cycle and oxidative phosphorylation of acetyl-CoA, giving $CO_2$ as the end product (96, 97).

### 3.1.1 D-glucose transport and metabolism in cancer

In the absence of sufficient oxygen, pyruvate is instead metabolized into lactate, in so-called anaerobic glycolysis, and only two ATP per D-glucose are produced. Cancer cells, due to higher metabolic rate, change from oxidative to mainly anaerobic metabolism, a process referred to as the Warburg effect (98). This favours cell division but produces significantly less energy per glucose molecule (only two ATP per glucose molecule). The Warburg effect leads to an increased glucose demand in tumours, to an overexpression or upregulation of GLUTs in tumour cells (99, 100), and to increased vascularization and thus a higher blood volume in the tumour. The rate of glucose influx can be 20-30 times higher than in normal cells (96). As will become clear in the next chapter, two consequences of the Warburg effect are particularly relevant from a glucoCEST point of view, i.e. (i) the increased lactate production, which lowers pH in the regions surrounding the tumour cells (the EES) but not in the cells themselves, and (ii) the increased glucose demand of the tumour, together with the increased vascular volume.

### 3.1.2 Regional glucose concentrations

Under steady-state conditions, the D-glucose concentration in brain tissue is around 20-25% of that in arterial plasma (79, 88, 101). However, in the case of malignancy, such as brain tumours with BBB breakdown, more glucose may enter the brain tissue via free diffusion, leading to an increased D-glucose concentration, especially in the EES. Separate estimation of extra- and intracellular concentrations is complicated with methods such as MRS and PET, and most studies have only estimated total brain tissue concentrations. This will be further discussed in Chapter 8.

Intracellular D-glucose concentrations can be measured in single cells by nanosensors (87). Zhang et al. used a polymer-based glucose sensor to measure intracellular D-glucose concentrations in vitro (102) (HeLa cells) at two different extracellular concentrations, 10 mM and 25 mM. Initially, starved cells had an intracellular D-glucose concentration of 0.12 mM, which later increased to 0.20 mM at both extracellular concentrations. In astrocytes, intracellular D-glucose concentration has been estimated to $0.63\pm0.30$ mM using a protein-based glucose sensor and 2 mM extracellular D-glucose concentration (87).

The D-glucose concentration in cerebrospinal fluid (CSF) is linearly related to the plasma D-glucose concentration (103) and can reach 15 mM under hyperglycaemic conditions (104). The CSF to plasma D-glucose ratio is around $0.6 - 0.65$ (103), and this ratio increases at hypoglycaemia, but is not affected by hyperglycaemia (103). Similar to blood-to-brain D-glucose transport, the D-glucose transport route from blood to CSF is believed to be carrier-mediated (104) and saturable (105).

# 4. GlucoCEST

As introduced in Chapter 2, CEST MRI is a novel MR imaging approach that combines the specificity of MRS with the sensitivity of MRI. It allows for detection of any compound with exchangeable protons, opening the door for using endogenous or exogenous natural compounds as MRI contrast agents. One such compound is D-glucose, which is promising as a contrast agent due to its biodegradability and kinetic properties, as described in Chapter 3. In this chapter, CEST and D-glucose will be combined, and the result is glucoCEST, the method that is the cornerstone of this thesis. The use of sugars as CEST contrast agents will be discussed in this chapter, while the application and implementation of glucoCEST in humans will be introduced in Chapter 6.

## 4.1  Glucose as a CEST contrast agent

D-glucose is the most frequently used sugar in DGE MRI. It is the same sugar that exists in the food that most of us eat every day, and it is also approved for intravenous injection in, for example, glucose tolerance testing. Hence, the emphasis of this chapter will be on the use of D-glucose as a CEST contrast agent. As will be seen by the end of this chapter, CEST using glucose analogues has been proposed, but these methods are still in their infancy, mainly due to potential toxicity or lack of FDA-approval.

### 4.1.1 D-glucose

D-glucose, the naturally occurring form of glucose ($C_6H_{12}O_6$), has five exchangeable -OH protons. The chemical shift differences and the exchange rates for the -OH protons are summarized in Table 4.1. The exchange rates are in the intermediate to fast exchange regime at the common magnetic field strengths used for human CEST imaging (3 and 7 T), leading to coalescence of all the glucose -OH proton resonances (25, 106). This violates Eq. 2.2 and is one reason for the low glucoCEST effect at 3 T compared to higher field strengths.

D-glucose occurs in a cyclic form and thus two anomers, differing in the direction of how one of the -OH groups is placed on the first carbon. These anomers, referred to as

alpha (α) and beta (β), have different chemical shifts, and the ratio α:β is 0.36:0.64 (106, 107), but depends on the pH and temperature of the glucose solution.

**Table 4.1.** Chemical shift offsets (Δω) and exchange rates ($k_{ex}$) for the -OH protons in D-glucose at 37°C and two different physiological pH levels. Data from Zaiss et al. (106).

| Δω [ppm] | Δω [rad/s] at 3 T | Δω [rad/s] at 7 T | Δω [rad/s] at 11.7 T | $k_{ex}$ [s⁻¹] pH 6.8 | $k_{ex}$ [s⁻¹] pH 7.2 | Number of -OH groups |
|---|---|---|---|---|---|---|
| 0.66 | 500 | 1200 | 2100 | 1500 | 2900 | 1 |
| 1.28 | 1000 | 2400 | 4000 | 3100 | 6500 | 3 |
| 2.08 | 1800 | 4100 | 6900 | 2500 | 5200 | 0.36 * |
| 2.88 | 2300 | 5400 | 9000 | 6000 | 14300 | 0.64 * |

* Due to two different anomeric conformations.

Because of the fast exchange, the hydroxyl resonances, which would be seen as troughs in the Z-spectrum at 0.66, 1.28, 2.08 and 2.88 ppm, cannot be detected at 3 T at physiological pH. Instead, all the glucose hydroxyl protons will together cause an asymmetric broadening in the line shape of the Z-spectrum (25), as illustrated in Figure 4.1. In other CEST approaches, such as APTw MRI, MTR$_{asym}$ analysis (Eq. 2.3) is commonly used to remove other magnetization transfer effects as well as direct water saturation contributions. Due to the coalescence of glucose with the water resonance frequency, leading to the appearance of D-glucose effects also on the negative side of the Z-spectrum (25, 106), asymmetry analysis is not the optimal choice of method in glucoCEST imaging since it would reduce the effect size. However, by studying the signal at one particular frequency offset before and after D-glucose administration, for example, by selecting 2 ppm, it becomes evident that in principle only a single saturation frequency offset is needed for glucoCEST imaging, as illustrated in Figure 4.1.
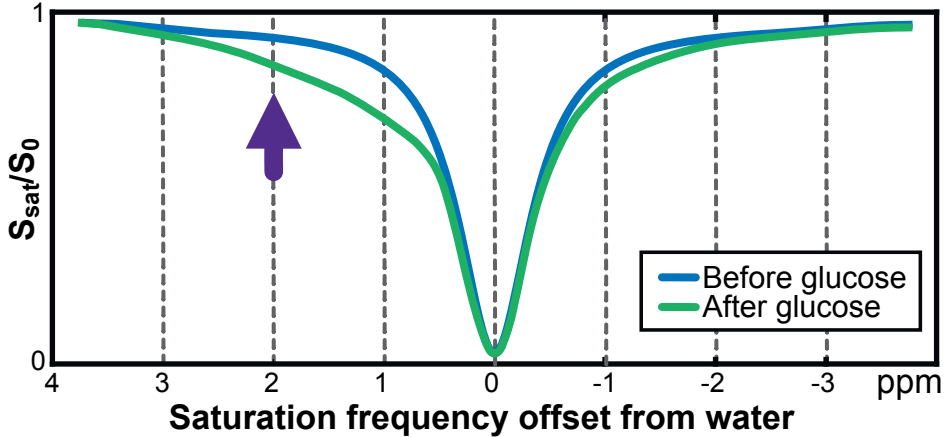
**Figure 4.1**. Illustration of a Z-spectrum measured before and after glucose administration. When the glucose concentration is increased, the Z-spectrum is broadened (exaggerated in this illustration), and a difference can be measured at the approximate resonance frequency of glucose (arrow).

In a typical glucoCEST experiment, D-glucose is given intravenously during image acquisition, allowing for dynamic detection of the signal change caused by D-glucose. This is referred to as dynamic glucose enhanced (DGE) (20, 21) MRI. An experimental setup for DGE MRI is illustrated in Figure 4.2. One or more non-saturated images $S_0$ are acquired, followed by images saturated at one chosen frequency offset, for example, 1.2 or 2.0 ppm for D-glucose. After a predefined time period, D-glucose is injected. The images before the start of the injection are averaged to form a baseline image.
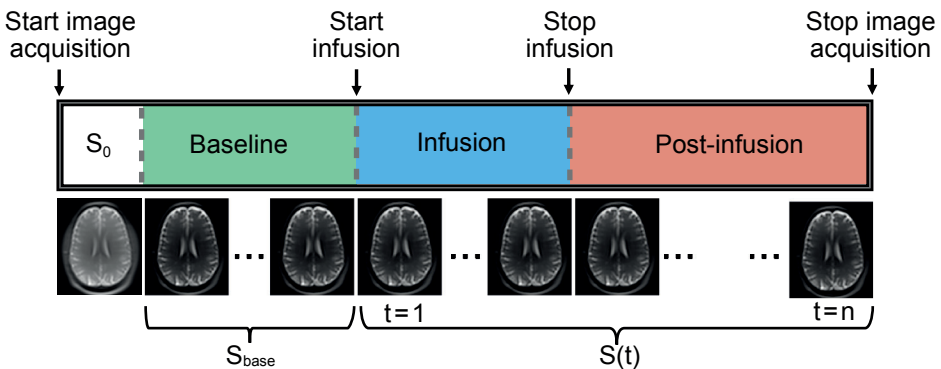


**Figure 4.2**. Schematic illustration of a typical acquisition of DGE MRI data. The protocol can be divided into four blocks: the white block represents collection of non-saturated image(s) $S_0$. Thereafter saturation is applied at the resonance frequency of glucose (often 1.2 or 2.0 ppm) for the rest of the acquisition. Initially, pre-infusion (baseline) images are acquired (green). Subsequently, glucose is injected over 1-4 minutes (blue), followed by a post-infusion period (red).

DGE maps are usually calculated by taking the difference between the baseline $S_{base}$ and each post-infusion image $S(t)$, normalized to $S_0$ or $S_{base}$, as explained by Figure 4.3 and Eq. 4.1.

$$\Delta\text{DGE(t) [\%]} = \frac{S_{base} - S(t)}{S_0 \text{ or } S_{base}} = \frac{\Delta S(t)}{S_0 \text{ or } S_{base}} \cdot 100\% \,, \qquad \text{(Eq. 4.1)}$$

In this manner, the signal change caused by D-glucose can be studied as a function of time. Figure 4.3 also includes an illustration of such a dynamic response curve.

A simple analysis approach commonly used in DGE MRI is to calculate the area-under-curve (AUC) of the DGE MRI signal for a time interval $\Delta t = t_2 - t_1$, as shown in Eq. 4.2.

$$\text{AUC} = \sum_{t_1}^{t_2} \Delta\text{DGE(t)} \ \text{ or } \text{AUC}_{\text{mean}} = \frac{1}{N}\sum_{t_1}^{t_2} \Delta\text{DGE(t)} \,, \qquad \text{(Eq. 4.2)}$$

where $N$ is the number of images in the time interval $\Delta t$.

In DGE maps, a positive signal change represents an increased D-glucose concentration in the voxel. As indicated by Eq. 2.1a, the signal change is assumed to be proportional to the change in D-glucose concentration, at least at the concentrations relevant for in vivo DGE imaging (17, 40). At higher concentrations, the situation is complicated by back-exchange of saturated protons, limiting the effect on the water signal (57). However, as mentioned above, the exchange rate depends on pH (44). A lower pH level results in a higher glucoCEST effect, since the exchange rate will decrease towards the more favourable intermediate exchange regime, allowing for more effective saturation. This is apparent from Table 4.1 and signifies that even if two regions have similar D-glucose concentrations, different DGE MRI signals can be measured if the pH levels differ between these regions. While this complicates the relationship between D-glucose concentration and CEST-signal, the pH dependence can also be advantageous in, for example, tumour visualization, where most signal originates from the extravascular extracellular space, which often has a lower pH due to cellular export of lactate (17, 108).
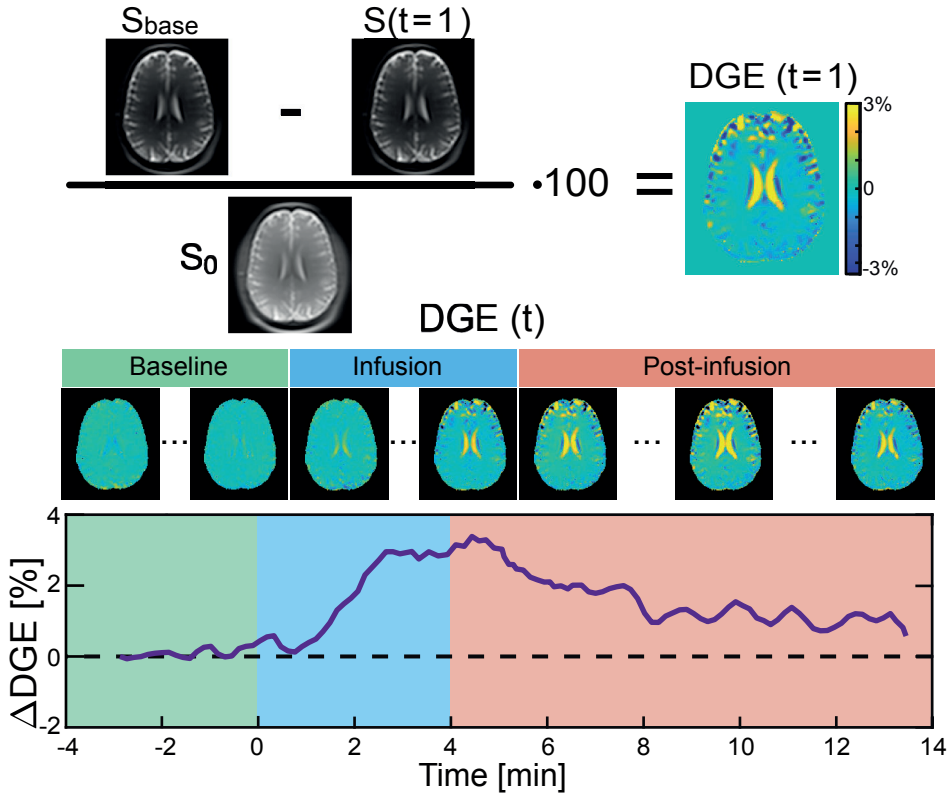
**Figure 4.3**. Illustration showing calculation of DGE images. All images, saturated at one selected frequency, are first normalized to a non-saturated image ($S_0$). The pre-infusion images are then averaged to one baseline image, and each saturated image in the time series is subtracted from this averaged baseline image. In the resulting DGE map, the signal change compared to baseline is shown, and positive values represent an increase in D-glucose concentration. A dynamic response curve (bottom) can then be measured in a voxel or region of interest.

As discussed in Chapter 2, the CEST effect also depends on $B_1$. A higher $B_1$ increases the CEST effects but also increases contributions from direct saturation and MTC, seen as a broadening of the Z-spectrum (36), also shown in Figure 2.2. The strength of $B_1$ would also potentially be restricted by SAR limitations in vivo and duty cycle limitations of the hardware. The optimal $B_1$ for DGE MRI depends on the experimental settings, for example, saturation frequency offset and saturation duration, so a higher $B_1$ can typically be used at higher magnetic field strengths because of the reduced interference from direct water saturation (25). Paper II included optimization of the DGE MRI protocol at 3 T, in terms of saturation frequency offset and $B_1$, as well as D-glucose infusion duration. This will be further discussed in Chapter 6. To date, no consensus for glucoCEST MRI has been established, but optimal saturation

schemes for different field strengths, based on simulations, have been published (25, 106).

The chemical exchange between D-glucose and water affects the observed transverse relaxation rate, $R_2 = 1/T_2$, of water, in that $T_2$ decreases with increased D-glucose concentration (109, 110). This results in a broadening of the Z-spectrum upon glucose administration, as illustrated in Figure 4.1. An advantage of the DGE MRI approach over the asymmetry analysis is that this symmetric contribution will be preserved in the calculation of $\Delta DGE(t)$, which will increase the measured DGE MRI signal. This is especially important at lower field strengths, where the coalescence of the glucose resonances with water is more pronounced. The single saturation frequency offset approach also improves the temporal resolution significantly, allowing for measurement of dynamic response curves.

As we will see in Chapter 5, the compartmental origin of the glucoCEST signal in vivo is not yet fully established, and sugars other than D-glucose may facilitate the elucidation of the origin of the glucoCEST signal. It is therefore relevant to briefly address the properties and kinetics of some other sugar types in this context (see also later chapters). The molecular structures of the introduced sugars are shown in Figure 4.4.
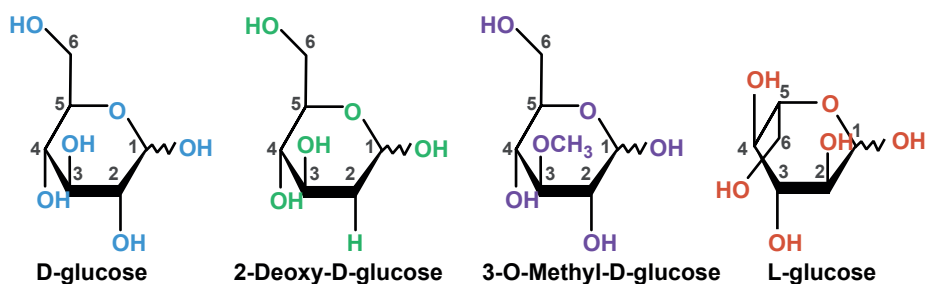


**Figure 4.4**. Chemical structures of four sugars that can be used as contrast agents in CEST MRI. D-glucose ($C_6H_{12}O_6$), 2-Deoxy-D-glucose ($C_6H_{12}O_5$), 3-O-methyl-D-glucose ($C_7H_{14}O_6$), and L-glucose ($C_6H_{12}O_6$).

## 4.1.2 2-deoxy-D-glucose (2-DG)

The 2-deoxy-D-glucose (2-DG) ($C_6H_{12}O_5$) type is similar to D-glucose, with just one structural difference in that the hydroxyl group on the second carbon is replaced by a hydrogen atom. 2-DG is initially carried through the same transport steps and metabolic pathways as D-glucose, but after phosphorylation by hexokinase to 2-deoxyglucose-6-phosphate (2-DG-6P) in the cell, it cannot be metabolized further. The

reason is that the difference in structure prevents isomerisation to fructose-6-phosphate and therefore halts the metabolism (111).

^{18}F-FDG, or 2-deoxy-2-[^{18}F] fluorodeoxyglucose is a deoxyglucose analogue that is similar to 2-DG, but the hydroxyl group which is replaced by hydrogen in 2-DG is instead replaced by the radionuclide fluorine-18. FDG also stops after phosphorylation to FDG-6P, and a so-called lumped constant is used in kinetic analysis of PET data to account for the different transport and metabolic properties of D-glucose and FDG. In general, the accumulated FDG-6P (or basically the measured radioactivity) at a certain timepoint post-infusion is assumed to be proportional to the glycolytic rate (i.e. the metabolism). Hence, both FDG and 2-DG reflect metabolism, and high-grade tumours typically show a higher concentration of 2-DG-6P and FDG-6P, due to their high glucose demand leading to increased GLUT expression and hexokinase action.

Both 2-DG and FDG compete with D-glucose for the available hexokinase and will therefore eventually inhibit glycolysis, since 2-DG-6P is accumulated in the cell. This will inhibit the metabolism of D-glucose and therefore ultimately induce cell death. These sugars are therefore toxic and can only be administered in trace amounts in humans. Hence, they are not suitable as CEST contrast agents (112), because of the high doses needed to obtain sufficient CEST effect. Nevertheless, 2-DG has been used in preclinical CEST (113) and CESL (114) MRI studies.

## 4.1.3 3-O-methyl-D-glucose (3-OMG)

The 3-O-methyl-D-glucose (3-OMG) ($C_7H_{14}O_6$) type is structurally similar to glucose, but has one methyl group (-$CH_3$) instead of the hydrogen of the third -OH group. It uses the same transporters as D-glucose and will therefore compete with glucose over the available transporter proteins. Hence, administration of 3-OMG can lead to a transient decrease in D-glucose concentration in the EES (112). 3-OMG is not phosphorylated but accumulates in the cell after transport, as well as in the EES. 3-OMG can therefore be used to assess glucose transport over the BBB and into the brain (115), and to measure steady-state tissue glucose concentration (81).

3-OMG has been used as a contrast agent for dynamic preclinical CEST imaging of breast tumours (116) and brain tumours (117) in mice. In the latter study, the contrast enhancement in tumour was approximately twice as high for 3-OMG as for D-glucose. 3-OMG is considered non-toxic (112) and has been used to study intestinal permeability in both paediatric patients and adults (118, 119). However, in these studies the doses were lower than those required in a CEST experiment. The potential toxicity or adverse effects at higher doses must be evaluated before 3-OMG can be used for CEST imaging in humans (57).

## 4.1.4 L-glucose (L-glc)

L-glucose is an enantiomer of D-glucose and has the same chemical formula, $C_6H_{12}O_6$, but cannot be transported by GLUTs. Hence, L-glucose has limited BBB permeability, it only enters EES through leakage, and it does not become metabolized as it cannot enter cells. It can therefore be used as an indicator of BBB breakdown, in resemblance to gadolinium-based contrast agents. L-glucose tastes like D-glucose (normal sugar) and was therefore once proposed as a low-calorie sweetener, but it is a strong laxative and is thus not suitable for use as a contrast agent in humans. It also reduces haematocrit and blood viscosity (120). However, similar to 2-DG and 3-OMG, L-glucose has been used in preclinical CEST (113) and CESL (114) studies.

# 5. The compartmental origin of the glucoCEST signal

The glucoCEST signal in vivo can hypothetically originate from three different compartments: the vascular compartment, the EES and the intracellular space. The relative contributions to the glucoCEST signal from these compartments are not fully established and the question whether glucoCEST reports on perfusion/permeability (vascular and/or EES origin) and/or metabolism (intracellular origin) still needs to be resolved. The compartmentalization of the different sugars introduced in Chapter 4 is schematically illustrated in Figure 5.1, for both healthy brain and tumour. In the study reported in Paper IV, we created a program for simulating compartmental concentrations as a function of the change in plasma concentration over time, also shown in Figure 5.1. The theory behind this model will be described in more detail in Chapter 8.

A vascular glucoCEST signal origin seems intuitively likely, since the blood D-glucose concentration is highest in this compartment and the D-glucose extraction fraction in the brain is small (around 11%) (81, 82, 88). It should be kept in mind that DGE imaging reflects the *change* in D-glucose concentration compared to baseline. Hence, if the D-glucose metabolism is constant and saturated already at baseline glucose concentrations, it is reasonable to assume that the change in intracellular glucose concentration would be close to zero, since the transport over the cell membrane is governed by metabolic requirements and transporter availability and not by the extracellular concentration. Indeed, in vivo studies using D-glucose have indicated that the DGE MRI signal is of vascular and/or extracellular origin (17, 21, 121, 122). In the studies described in Papers I & II, arterial input functions were measured in DGE data, and the results confirm the presence of a vascular contribution in the glucoCEST signal. In one of the first glucoCEST studies (17), Chan et al. used a preclinical mouse model of two human breast cancer cell lines, one highly malignant and one less aggressive. GlucoCEST images were compared to FDG-PET and gadolinium contrast-enhanced MRI, and only glucoCEST provided a significant difference between the two tumour types. The glucoCEST signal was lower in the more aggressive tumour type, indicating that glucoCEST does not represent intracellular D-glucose. The higher CEST signal in tumours than in normal tissue was attributed to the increased vascular and EES volumes and to the lower pH in the EES. The contribution from the

intracellular compartment was stated to be negligible due to the rapid metabolism in solid tumours and the low concentration of D-glucose and intermediate sugars in the breakdown pathway (glycolytic chain).
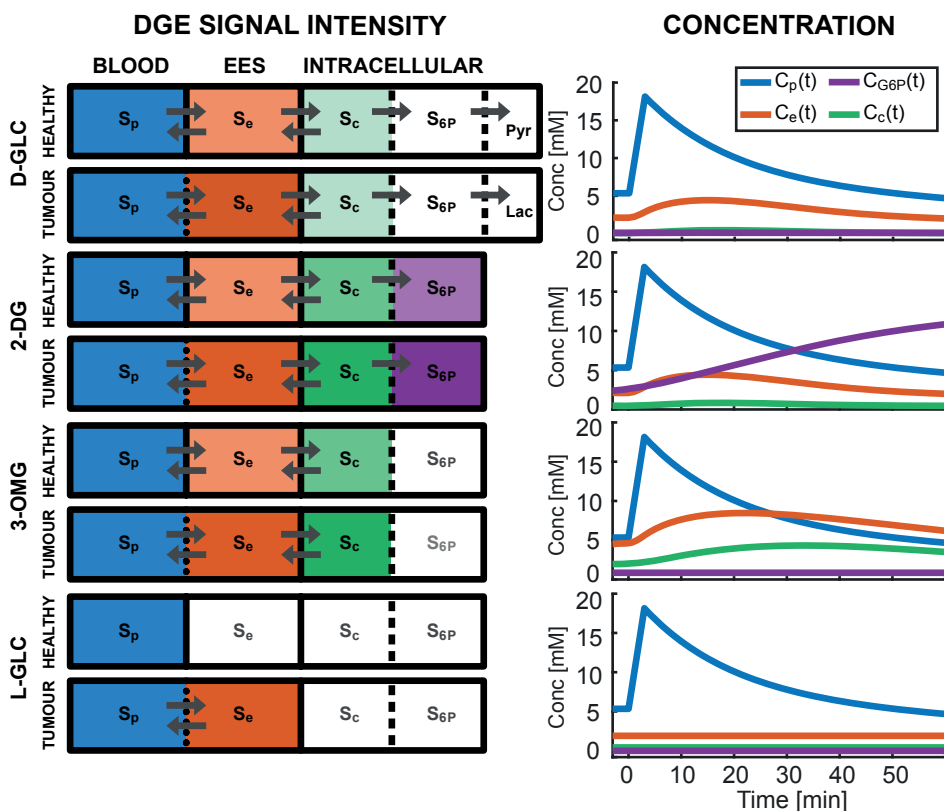


**Figure 5.1**. Illustration of the compartmental origin of different sugars (D-glucose, 2-DG, 3-OMG and L-glucose). Left panel shows DGE MRI signal intensity in both healthy tissue and tumour, while the right panel shows concentration (C) of sugar in plasma (p), EES (e), intracellular space (c), as well as intracellular concentration of phosphorylated sugar (G6P) as a function of time in healthy tissue only. S for signal: black for contributing, grey for no or negligible signal contribution. Solid lines represent actual borders (BBB or cell membrane, dotted line for broken BBB). Dashed lines represent a metabolic border, and the arrows represent transport over a border. A darker color denotes a higher relative signal contribution.

Xu et al. used DGE MRI with D-glucose to study increased blood volume and BBB breakdown in a preclinical brain tumour model (21). The DGE MRI signal was higher in tumours than in contralateral brain, allowing for separation of tumour and healthy tissue. For comparison, dynamic contrast enhanced (DCE) MRI, that normally employs a rapid intravenous injection of a gadolinium contrast agent during imaging,

was also performed. When comparing response curves from DGE and DCE MRI, it appeared that D-glucose enters the EES more rapidly and that DGE MRI may be favourable for BBB breakdown detection. Due to the rapid metabolism, the intracellular CEST signal was assumed to be negligible, and the measured DGE MRI signal in tumours was concluded to originate from the EES and vessels. In an additional preclinical glioblastoma model, Xu et al. used rapamycin and D-glucose to further investigate the signal origin of glucoCEST (121). Rapamycin treatment reduces the cellular metabolism and D-glucose uptake, which will increase the signal contribution from the vascular compartment and the EES. The post-treatment DGE MRI signal change was higher in both brain tissue and vessels, indicating that the glucoCEST signal originates mainly from the EES and the vascular compartment, with minimal contribution from the intracellular compartment (121).

In another early glucoCEST study, Walker-Samuel et al. performed an in vitro experiment and could show that sugars in the early stages of glycolysis can be detected with glucoCEST in a phantom, especially G-6P which gave a similar enhancement as D-glucose (18). This makes sense in phantoms at the same concentrations, but in vivo intracellular concentrations are lower. GlucoCEST could be used to distinguish between two tumour types with different metabolic activity in mice. There was a correlation between [18]FDG and glucoCEST, but not between gadolinium and glucoCEST, leading to the conclusion that glucoCEST after D-glucose injection also reports on metabolism. Researchers in another preclinical glucoCEST study (113) administered D-glucose, L-glucose and 2-DG in mice. As introduced in a previous chapter and in Figure 5.1, L-glucose will mainly circulate in the blood, while 2-DG enters cells and undergoes the first step of glycolysis, leading to intracellular accumulation of 2-DG-6P. These experiments showed that the CEST signal increased with 2-DG concentration but decreased when cerebral metabolism was suppressed. D-glucose resulted in a lower glucoCEST signal than 2-DG, and L-glucose did not produce any glucoCEST signal. Additionally, the 2-DG and D-glucose CEST response curves did not correlate with blood glucose concentration. Altogether, the conclusion in this study was that the glucoCEST signal is mainly originating from sugars and phosphorylated sugars in the intracellular compartment, but that further studies are needed to determine the compartmental origin of glucoCEST.

Recently, Eleftheriou et al. investigated the compartmental contributions to the DGE MRI signal using fibre photometry of a glucose sensor in combination with CEST imaging of D-glucose, 3-OMG and L-glucose in mouse brain (122). All three sugars resulted in an increased DGE MRI signal upon administration. The results suggest that the initial rise of the DGE curve originates from EES and vessels, and that the relative compartmental contribution depends on the time after glucose injection. The authors attributed the difference between the L-glucose results in their study and in the study by Nasrallah et al. (113) to the different analysis methods used. Nasrallah et al. used

MTR$_{asym}$, while Eleftheriou et al. used the subtraction (single-offset) method. As mentioned in Chapter 4.1, ΔDGE analysis retains the symmetric contribution from T2 relaxation of glucose, while the MTR$_{asym}$ approach does not. Additionally, kinetic modelling revealed that a vascular component is needed to describe the initial rise in the measured D-glucose DGE curve.

The project in Paper III included studies of response curves from DGE and DCE MRI acquired at 7 T in patients with brain tumours (mainly glioblastoma). Plateauing curve shapes and a higher DGE MRI signal were found in tumour compared to normal tissue in some patients, but not in all. This observation was probably reflective of BBB breakdown and lower extracellular pH, i.e. dominated by D-glucose in the EES. Additionally, a remarkably high DGE MRI signal was found in one patient that turned out to have a cavernoma, not a tumour. Cavernomas often have a large volume of slowly flowing blood, and this finding confirms that the DGE MRI signal includes contributions from the vascular compartment. As discussed in Paper III, D-glucose and gadolinium exhibit different tissue uptake kinetics and the DGE and DCE MRI signals have different compartmental origins. The DCE MRI signal has compartmental contributions similar to L-glucose in Figure 5.1. When comparing DGE and DCE MRI enhancement patterns, we found that DGE MRI sometimes enhanced tumour regions not enhanced by gadolinium. The reason for this can be related to lower pH in EES, leading to a change in DGE but not in DCE MRI signal, since the latter is not sensitive to pH. Alternative explanations are the facilitated transport of glucose, meaning that the glucose concentration may increase in the EES also in regions with an intact BBB, where gadolinium does not have access. The plateauing and continuously increasing curve types could indicate a contribution from glucose metabolites, such as G-6P or lactate, in the cells. However, the signal was monitored for a time too short (12 minutes from the start of the infusion) to give any clear answers to this. In the context of the compartmental origin of the DGE MRI signal, the findings described in Paper III indicated a vascular, extravascular extracellular, and, at later time points, perhaps also an intracellular contribution.

The compartmental origin of signals from different sugars has also been studied with glucoCESL. Jin et al. compared dynamic CESL using D-glucose, 2-DG and L-glucose to DCE MRI in a rat brain tumour model (114). CEST is more sensitive to pH (favoured by a slower exchange rate of the -OH protons) than CESL. This leads to similar weightings of intracellular and extracellular glucose in CESL, and the results of this study are not necessarily representative for glucoCEST. In any case, the main conclusion from this study was that the glucoCESL signal has both intra- and extracellular contributions. A re-assessment by Knutsson et al. concluded that the signal was mainly originating from blood and EES because the tumour signals for L-glucose and D-glucose were equivalent for the first 10 minutes post-injection, after which D-glucose became lower, presumably due to metabolism (57).

In conclusion, the human glucoCEST experiments performed so far have not led to any clear conclusions on this topic. The reasons are probably a combination of the low DGE MRI signal in vivo, the limited number of patients/healthy volunteers examined in each study, and the absence of a complete kinetic model for DGE MRI. As discussed in Chapter 8 and Paper IV, the different potential compartmental signal origins must be considered when developing kinetic models for glucose delivery and uptake, and these models, on the other hand, may help reach a conclusion on this topic.

# 6. GlucoCEST in humans

As mentioned previously, the endogenous brain D-glucose concentrations are difficult to estimate from the CEST signal at clinical field strengths due to background CEST, MTC, and direct saturation signal contributions. The common approach in glucoCEST MRI is therefore to perform dynamic difference imaging before, during and after D-glucose injection. In this chapter, the technical aspects of applying glucoCEST using D-glucose in humans are reviewed. Optimization and development of the glucoCEST method are discussed, as well as the choice of glucose infusion protocol.

The first human glucoCEST results were published in 2015, demonstrating the feasibility of DGE MRI to study BBB breakdown and to enable separation of tumour from normal tissue at 7 T (20). Since then, DGE MRI has been applied to healthy brain and brain tumours at 7 T (22, 24, 123, 124), and has made progress towards clinical imaging by showing feasibility for DGE MRI of brain tumours and healthy volunteers at 3 T (25, 26).

## 6.1 Optimization and challenges of DGE MRI

DGE MRI is difficult to optimize since the results depend on imaging and saturation parameters as well as the D-glucose infusion protocol. For improved reproducibility of the baseline level, the healthy volunteer or patient should preferably be fasting several hours before the examination. Normoglycaemia is a requirement for injection of D-glucose. For example, in Papers I – III a fasting blood glucose level in the range 3.9 – 7.5 mM was used as an inclusion criterium. After injecting D-glucose, the blood glucose level will be elevated for a few hours, and another injection cannot be performed during this time. Consequently, only one DGE MRI experiment per subject per day is recommended. The choice of imaging and saturation parameters reported in Papers I – III were based on simulations and on previous studies (20, 25)

## 6.1.1 Technical aspects

The major challenge in glucoCEST imaging is the small CEST effect, being only a few percent at 7 T and even lower at 3 T, caused by the coalescence effects discussed in Section 4.1. The small signal change and the use of signal subtraction (ΔDGE calculation) make DGE MRI prone to motion artefacts. Non-CEST-related signal changes can arise in DGE maps due to motion, especially seen at tissue interfaces, but also due to motion-induced $B_0$-shifts. These occurrences can lead to signal changes comparable in size to the actual DGE MRI signal, so-called pseudo-CEST effects (32). A change in $B_0$ will shift the Z-spectrum in a given voxel to the left or right relative to the water resonance, as illustrated in Figure 6.1. Consequently, changes in $B_0$ over time, due to scanner drift or motion-induced changes in local magnetic field, will, if not corrected for, result in an erroneous CEST signal change (125). Different methods for dynamic $B_0$ correction have been proposed, all requiring additional scanning time when compared to the simple single-offset DGE MRI approach. One method is to collect Z-spectra and shift the DS minimum of each (interpolated or fitted) spectrum in each voxel back to the water frequency (126). Another approach is to retrieve separate $B_0$ maps from phase images and use these to shift back the Z-spectrum (127). The correct Z-spectrum position can also be found by the water saturation shift referencing (WASSR) technique, in which a low $B_1$ and short saturation Z-spectrum centred narrowly around the water resonance is acquired and used to identify the absolute water frequency in each voxel (128).



**Figure 6.1.** Illustration exemplifying how the Z-spectrum is affected by $B_0$ inhomogeneities. A change in $B_0$ will shift (green arrows) the Z-spectrum away (solid line) from its initial position (dashed line). This will result in an erroneous CEST signal at the DGE MRI measurement position (blue arrow).
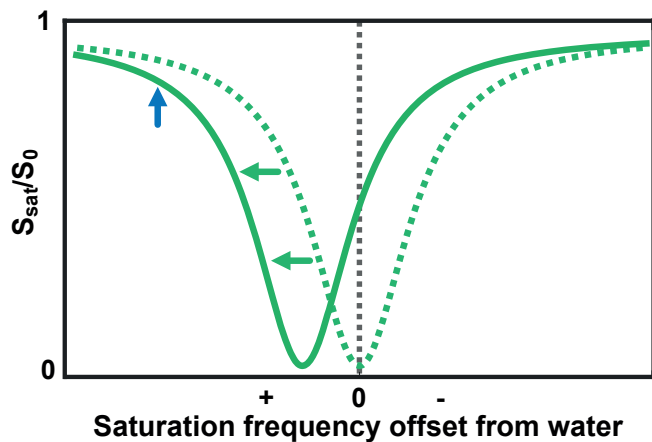
However, none of these methods are suitable for single-frequency DGE imaging, since multiple acquisitions in terms of several points of the Z-spectrum are needed. In the work of this thesis, high temporal resolution (Papers I and III) or volume coverage (Paper II) were prioritized using the single saturation frequency offset approach.

Dynamic $B_0$-correction was therefore not implemented. However, dynamic $B_0$-correction would have improved the DGE maps and helped the interpretation. The initial rationale for employing the single-offset DGE MRI approach was that the broad -OH resonance from D-glucose at further shift (2 ppm) from the water protons, i.e. at a point with a lower slope of the direct saturation signal curve, implies that the ΔDGE calculation is quite insensitive to $B_0$ inhomogeneities. Since then, we have become aware that this needs not be the case.

In the Paper II study, we compared DGE MRI protocols in healthy volunteers scanned at 3 T in order to confirm existing recommendations and establish additional ones. More specifically, two different saturation protocols, and two different infusion durations were evaluated. To estimate the magnitude and effect of $B_0$ shifts on the DGE MRI signal, WASSR images were collected before and after the DGE imaging. $B_0$ shift maps were calculated from the WASSR images in four healthy volunteers. The estimated $B_0$ shifts were at most around ±5 Hz. To estimate the effects of $B_0$ changes on the DGE MRI signal, simulations of Z-spectra were performed by numerically solving the Bloch-McConnell equations for two D-glucose concentrations corresponding to baseline and post-infusion. The simulated effects of $B_0$ changes on the DGE MRI signal in artery and white matter (WM) showed that the effect was larger for the 1.2 ppm/0.6 µT protocol (approximately 0.2%/Hz) than for the 2.0 ppm/1.6 µT protocol (approximately 0.1%/Hz) These results indicated that single saturation offset acquisition of glucoCEST images can be problematic, especially at saturation frequency offsets closer to the water resonance. One conclusion of Paper II was that a saturation frequency offset of around 2 ppm is recommended for single-offset DGE MRI at 3 T, instead of the 1.2 ppm offset commonly used at 7 T.

The importance of motion correction and mitigation has been stressed in recent DGE MRI studies (25, 26, 32, 125, 129). In the investigations reported in Papers I and III, single slice DGE MRI acquisition was employed, making correction for through-plane motions impossible. In these studies, residual motion was often evident, especially at tissue interfaces. An example of such residual motion is shown in Figure 6.2. The long scan times of a typical DGE MRI experiment may also be an issue, not only because of cost and patient comfort, but also because of the increased risk of motion artefacts. However, for dynamic studies, the tissue response needs to be followed for at least 5-10 minutes after the start of infusion, why focus on motion mitigation and especially development of more sophisticated motion correction techniques is warranted.
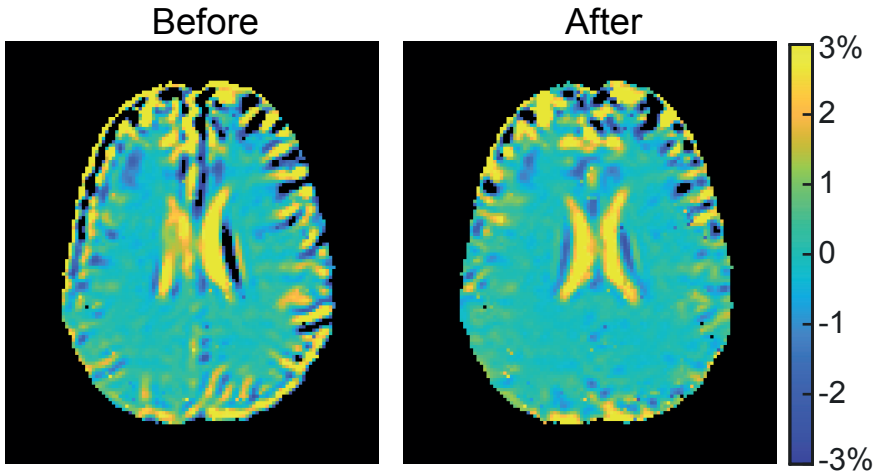
**Figure 6.2**. Post-infusion DGE maps from one experiment on a healthy volunteer at 3 T. Single-slice DGE MRI was acquired at 3 T and DGE maps were calculated using Eq. 4.1. The left image shows the original DGE map. Motion artefacts are seen as spatially alternating dark-bright patterns, especially at tissue interfaces and in regions containing CSF. The right image is calculated after realignment of the CEST images using a motion correction algorithm. The motion-induced patterns are reduced, but residual motion artefacts of the same order of magnitude as the expected DGE MRI signal can still be seen. This healthy volunteer was scanned in the study described in Paper II using the 2.0 ppm/1.6 µT protocol,. (Note, however, that the single slice data were not included in the final paper).

Additionally, tissue volumetric changes, for example, of the lateral ventricles, caused by physiological responses to D-glucose administration can deteriorate the DGE MRI signal (20, 25, 26, 125). Adverse effects of D-glucose infusion and suggestions on how to reduce these are described in Paper II, and will be further discussed in the subsequent section.

In the studies of Papers I-III, tissue response curves were measured in WM. The DGE MRI signal in WM was in many cases negative, which was consistent with previous observations (25, 26). This finding is puzzling and has not yet been fully explained. In Paper II, we report observations that the negative signal tended to recover towards the end of the time series, why it was concluded unlikely to have been caused by field drift. Negative DGE MRI signal is not expected but could be caused by a susceptibility-based frequency shift (25). In Paper II, we describe findings of a significant negative correlation between DGE MRI signal in WM and the change in venous blood glucose level in 50% of the volunteers, indicating that this effect is somehow related to the D-glucose injection. Hasselbalch et al. measured a significant increase in $CMR_{glc}$ in WM, but not in grey matter (GM), using dynamic FDG-PET at hyperglycaemia in humans (91). However, the authors did not provide any explanation for this finding, and it is still unlikely that such an increase in $CMR_{glc}$ would lead to a lower D-glucose concentration in WM at hyperglycaemia than at euglycemia.

In DGE MRI studies, the spatial resolution is often compromised in favour of temporal resolution and SNR. This makes DGE MRI sensitive to partial volume effects (PVEs), especially when measuring AIFs as in the studies described in Papers I and II. The interpretation of PVEs in DGE MRI is potentially complicated by tissue mixing of different Z-spectral line shapes, which may lead to erroneous hyper- or hypointensities, especially related to CSF.
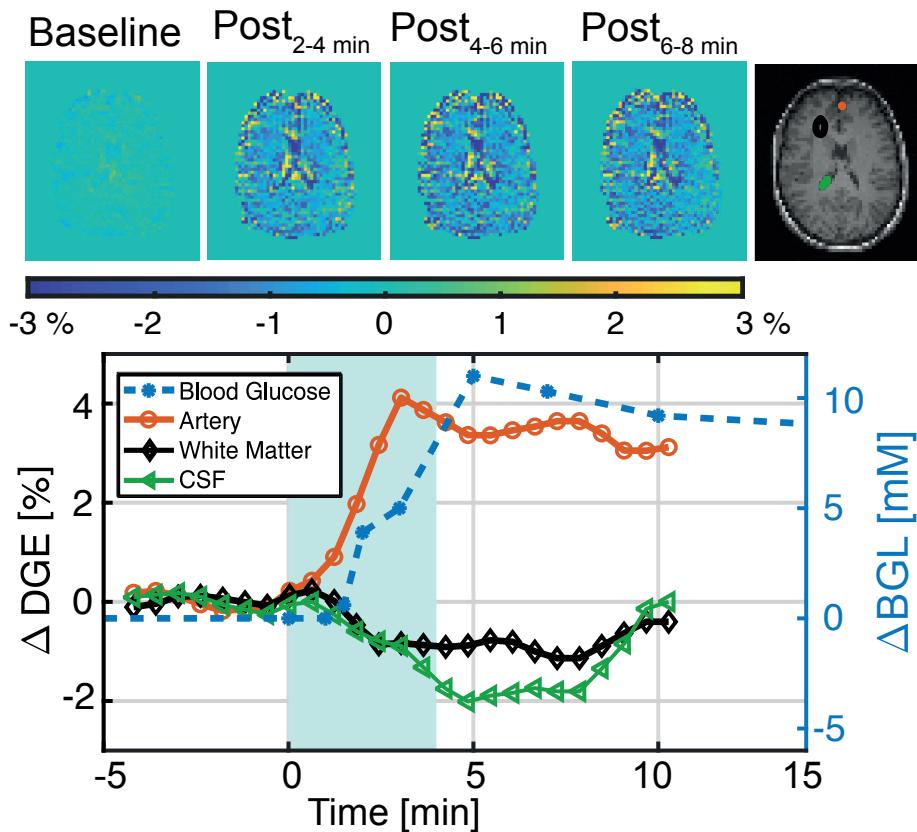


**Figure 6.3**. Top: ΔDGE AUC$_{mean}$ maps calculated from 2-min intervals taken before and after D-glucose infusion (4 minutes duration, shown in light blue), as well as an anatomical image with regions of interest (ROIs). Bottom: ΔDGE MRI signal in artery, white matter, and cerebrospinal fluid (CSF) ROIs together with the change in venous blood glucose level (ΔBGL) as a function of time. Figure adapted from Paper II, published by Wiley and licensed under CC BY 4.0.

## 6.1.2 Glucose administration

In a typical DGE MRI experiment, D-glucose is administered during imaging, raising the fasting blood glucose level of around 5 mM to 15 mM (20). The blood D-glucose

level starts to rise rapidly and peaks within a few minutes, depending on infusion rate and administration method, but also on individual differences in insulin response.

D-glucose can be administered into the blood stream by an intravenous (i.v.) injection, either manually or via a power injector. The word "infusion" is often used to differentiate this type of injection from the shorter bolus-like injections (lasting a few seconds) that are typically used in gadolinium imaging. The change in blood glucose level and insulin response after D-glucose infusion depends on the infusion rate (130). A faster infusion typically gives a quicker rise in venous blood D-glucose level, together with a faster insulin response and thus a faster subsequent decrease of the blood D-glucose level back towards the baseline value. The peak blood glucose concentration is not significantly affected by the infusion rate (130). Figure 6.4 shows averaged venous blood D-glucose levels from 25 healthy volunteers scanned in our different glucoCEST experiments, divided into three different infusion duration groups. The averaged curves indicate the same trend in that a shorter infusion tends to give a more rapid response and a steeper rise in venous blood D-glucose level, and that the maximum concentration seem to be independent on infusion duration. The choice of infusion duration for DGE MRI experiments was investigated according to Paper II and will be discussed later in this chapter.
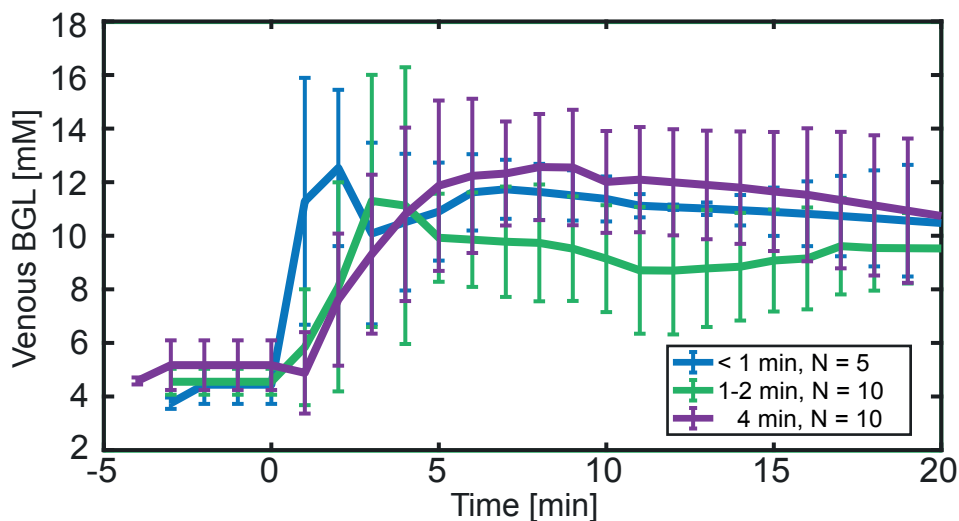


**Figure 6.4.** Influence of injection time. Averaged venous blood glucose level (BGL) measured in 25 healthy volunteers in our glucoCEST experiments. Figure based on data from Paper I and Paper II as well as additional measurements (not published), grouped according to infusion duration.

An advantage of intravenous infusion is that the response is quick, and the whole procedure can therefore be performed while imaging. A disadvantage is that differences in response among individuals may occur, and that insertion of a peripheral venous catheter is necessary.

An alternative intravenous administration approach is the hyperglycaemic clamp method, in which blood glucose is raised to a target level (for example, 15 mM) and then stabilized by repeatedly measuring the blood D-glucose level and adjusting the glucose infusion rate accordingly. An advantage of the clamp method is that a stable hyperglycaemic level is reached, potentially making kinetic modelling easier because a steady-state situation is reached in the blood. Another advantage is that D-glucose accumulates in the EES, because glucose transport across the BBB strives towards concentration equilibrium, in combination with a constant cerebral metabolic rate of glucose (131). While this appears to make it more difficult to distinguish normal brain from tumour, as D-glucose accumulates in EES of healthy and tumour tissue, it seems likely that a difference in extracellular pH may still allow such separation. A disadvantage is that the method is time-consuming and requires continuous collection of blood samples, and more surveillance, than a single injection.

Oral administration, typically via a drink with D-glucose, results in a slower response, as well as a higher insulin response (132). As illustrated in Figure 6.5, this leads to a smaller change in blood glucose level, which is not advantageous in a DGE MRI context. Oral administration is also practically difficult, because the subject has to either drink the glucose solution while lying in the scanner or be taken out and then repositioned. An advantage is that the oral method is non-invasive since no injection is needed.

Example responses in venous blood glucose and insulin levels after different D-glucose administration methods are depicted in Figure 6.5. The illustrations of the response curves are based on the following references: intravenous (130), our own experiments (Papers I & II), hyperglycaemic clamp (129, 133) and oral (132, 134, 135).



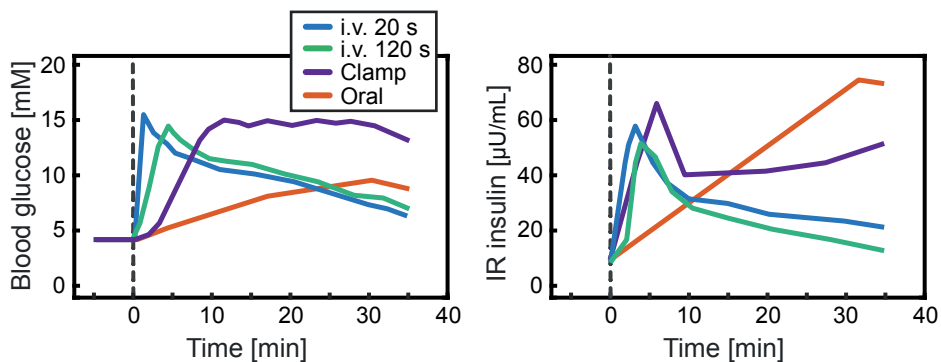**Figure 6.5.** Illustration showing how the blood glucose (left) and immunoreactive (IR) insulin (right) concentrations change after giving a typical dose of D-glucose using four different administration methods starting at time = 0. i.v., intravenous injection. IR, immunoreactive insulin, measured in $\mu$Units per mL (which is a common way of measuring the unbound and biologically active fraction of total blood insulin).

A potential challenge for future clinical implementation of glucoCEST is the increased fasting blood D-glucose level associated with some medications such as steroids used in cancer patients (57). This actually led to the exclusion of a few patients in Paper III and in our glucoCEST studies at 3 T (data not published).

Different D-glucose concentrations, doses and infusion durations used in human glucoCEST/CESL experiments are summarized in Table 6.1. There is currently no consensus regarding D-glucose concentration and doses in human experiments (57).

**Table 6.1.** D-glucose administration methods used in 14 human glucoCEST/CESL experiments.

| Conc. w/v | Dose | Volume | Admin. method | Duration | Reference | Year |
|---|---|---|---|---|---|---|
| 50% | 25 g | 50 mL | i.v. | 60-80 s | Xu et al.(20) | 2015 |
| N/A | N/A | 20 mL | i.v. | "Bolus" | Wang et al.(28) | 2016 |
| 20% | 20 g | 100 mL | i.v. | 6 min | Schuenke et al.(123) | 2017 |
| 20% | 20 g | 100 mL | i.v. | 2 min | Schuenke et al.(24) | 2017 |
| 20% | 20 g | 100 mL | i.v. | 2 min | Paech et al.(22) | 2017 |
| 50% | 25 g | 50 mL | i.v. | 23-65 s | Paper II | 2018 |
| 20% | 15-29 g | 74-145 mL | Clamp | 30-60 min | Kim et al.(129) | 2019 |
| N/A | 50 g | N/A | Oral | N/A | Luo et al.(27) | 2019 |
| 20% | 0.3 g/kg b.w. | N/A | i.v. | 2-2.5 min | Herz et al.(26) | 2019 |
| 50% | 25 g | 50 mL | i.v. | 63, 125, 167 s | Xu et al.(25) | 2020 |
| 20% | 20 g | 100 mL | i.v. | 2 min | Boyd et al.(124) | 2020 |
| 20% | 1 mL/kg b.w. | ~70 mL | i.v. | 2-2.5 min | Bender et al.(136) | 2021 |
| 50% | 25 g | 50 mL | i.v. | 4 min | Paper II | 2021 |
| 50% | 25 g | 50 mL | i.v. | ~1 min | Paper III | 2022 |

Admin. - administration; b.w. – body weight; Conc. - concentration; i.v. - intravenous; N/A - not available; w/v - mass concentration (weight/volume) in percent.

### 6.1.3 Physiological responses to intravenous glucose administration

D-glucose is promising as a biodegradable contrast agent, but the intravenous D-glucose injection used in most glucoCEST experiments is associated with side effects. In Paper I, we report that both sensory effects and physiological responses may occur. This was further investigated, as described in Paper II, and also reported by Xu et al. (25). The sensory side effects are transient and usually disappear within a few minutes but can be uncomfortable for the subject and may, consequently, generate movements. Physiological effects, such as volumetric changes of the ventricles caused by D-glucose uptake or pulsations, can produce DGE MRI signal changes that are not related to the CEST effect (125), complicating the DGE image interpretation. Additionally, D-glucose solutions ≥10% are hypertonic, and may therefore cause vein irritation and thrombophlebitis (137). The latter was reported by one volunteer in Paper II and by one volunteer in another glucoCEST study (129). It is therefore important to optimize the D-glucose infusion protocol for glucoCEST in terms of infusion duration and D-glucose concentration.

In the Paper I study, D-glucose was injected over 23-65 seconds. The reported sensory side effects related to the D-glucose infusion included a feeling of warmth, sugary taste in the mouth, transient heat flashes in the head and crotch and feeling an urge to urinate. All effects were short-lived and disappeared within a few minutes. Some of the side effects were attributed to the high osmolarity of the glucose solution (approximately 10 times higher than in blood). To restore osmotic pressure equilibrium, water is transported from the extravascular to the intravascular space, leading to an increase in intravascular pressure. A faster infusion tended to be associated with stronger side effects. In a further investigation (Paper II), DGE imaging was performed in healthy volunteers using different scanning protocols at 3 T, including two different infusion durations (1.5 and 4.0 minutes, respectively). The overall incidence and severity of the orally reported side effects of the D-glucose infusion was smaller in the group that had the longer infusion duration. All subjects in the short infusion group experienced one or more sensations after D-glucose infusion. These adverse effects were similar to the ones reported in Paper I, but with the addition of headache which was experienced by three out of four subjects. One subject in this group also reported a thrombophlebitis close to the injection site a few days after the examination. In the group that received the longer infusion, one third of the twelve subjects did not experience any side effects. The reported side effects in this group were mainly related to sensory experiences at the injection site. No significant difference in maximum change in blood glucose level between the 1.5 and 4.0-minute infusion groups was found. This was in line with the results by Chen and Porte, who studied responses in insulin and blood glucose levels to different infusion durations and doses (130). Altogether, the findings reported in Paper II indicated that a longer infusion duration than previously proposed should preferably be used in glucoCEST studies,

since it can minimize the side effects of the D-glucose infusion while not reducing the maximum blood glucose level and thereby preserving the DGE effect size.

It should be emphasized again that the sensory side effects are transient, and comparable to adverse effects related to injection of iodine-based contrast agents. On another note, it may seem counterintuitive that Paper III describes a shorter infusion duration than in Paper II. However, the reason being is that the patients in Paper III were scanned before the study in Paper II was conceived.

Physiological changes of the brain, especially volumetric changes of the lateral ventricles following D-glucose infusion, have been mentioned as a source of artefacts in DGE MRI (20, 26, 125). Puri et al. investigated the effect of oral glucose administration and found a dilatation of the lateral ventricles of 2.4% after oral glucose loading in six fasting healthy volunteers (138). To our knowledge, volumetric changes after intravenous D-glucose administration have not been extensively investigated. As shown in Paper II, we collected six anatomical 3D image volumes sequentially before, during and after D-glucose infusion in one healthy volunteer. The volume of the lateral ventricles was measured, and the volume change over time was compared to the change in venous blood glucose level. A volume increase of up to 2% was measured, which is comparable to the results of Puri et al. However, we studied only one volunteer, and the experiment should be repeated with a larger cohort in order to confirm reproducibility.

There are two types of volumetric changes of the lateral ventricles that may cause pseudo-DGE effects, i.e. dilatation caused by glucose administration and pulsations related to the cardiac cycle (125). These effects can, together with the relatively high glucose concentration in CSF (about 60% of the plasma concentration (104, 139)), create non-rigid volumetric changes that are difficult to correct for using a standard rigid motion correction algorithm (125). This can complicate interpretation of lesions situated in CSF-rich regions.

Despite these challenges, glucoCEST using D-glucose, or other sugars, has shown potential for tumour detection, and, as we will see in the following chapters, provides a rather unique possibility to non-invasively study glucose delivery, transport and metabolism.

# 7. Curve shape analysis

The tissue response curves measured in a dynamic imaging experiment can provide information about arrival, uptake, and disappearance of an injected contrast agent in a tissue of interest. The shape of the curve, for example the steepness of the initial rise and the slope of the washout can provide information about, for example, BBB permeability and vessel integrity.

There are three principal approaches for analysis of tissue response curves in DCE MRI, sometimes referred to as qualitative, semi-quantitative, and quantitative analysis (140). The simplest approach is based on visual assessment of curve shape, in a single pixel or region of interest (ROI). The shape of the curve can then be generalised as belonging to one out of three categories of curve shapes after the initial rise: decreasing, constant, or increasing, which in principle can be used to differentiate tumour regions from normal tissue regions (140). As an example, vascular disruptions are often characterized by a rapid uptake (141). As a more extensive alternative to visual curve shape assessment of ROIs or single pixels, a method relying on pixelwise classification of curve types has been introduced, referred to as time-intensity curve (TIC) shape analysis (141). TIC shape analysis of curve shape patterns has been applied predominantly to DCE MRI of breast tumours (142, 143), but also to prostate cancer (144), brain (145) and the musculoskeletal system (146).

The second DCE MRI analysis approach relies on calculation of parameters based on curve properties, such as area under curve (AUC), time-to-peak (TTP), maximum enhancement ($S_{max}$) and wash-in/wash-out slope ($S_{in}$ and $S_{out}$) (147), as illustrated in Figure 7.1. As an example, increased wash-in slope, AUC and $S_{max}$, and shortened TTP can be related to increased vascular density and permeability (140). Common for both these non-model-based analysis methods is that they are less complex than model-based analysis, because AIF measurement, conversion from signal to concentration, or assumptions regarding the underlying physiology are not needed.
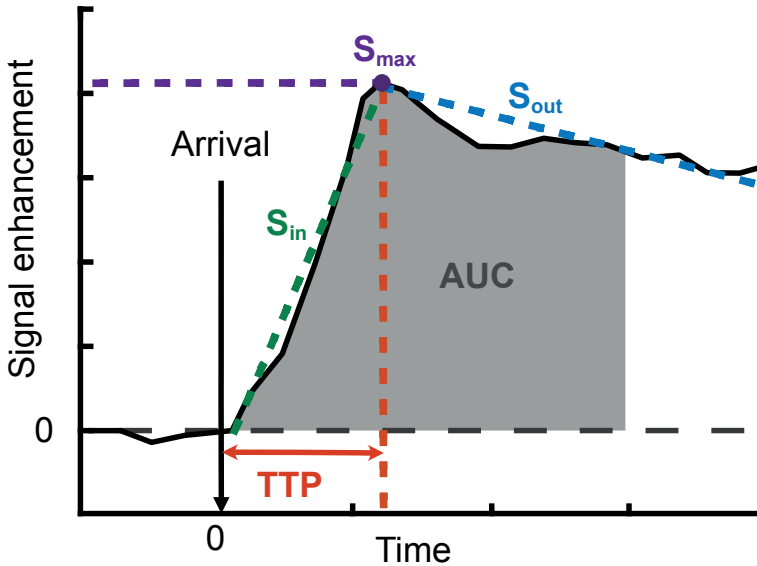
**Figure 7.1.** Illustration of common descriptive parameters that can be calculated in so-called semi-quantitative or non-model-based DCE MRI analysis. Area under curve (AUC), time-to-peak (TTP) denoting the time from the contrast agent arrival to the peak, maximum enhancement ($S_{max}$) and wash-in/wash-out slope ($S_{in}$ and $S_{out}$).

The third DCE MRI analysis method is tracer kinetic modelling, in which a biophysical model expression is fitted to the tissue response curves to retrieve quantitative parameters reflective of, for example, perfusion, vessel permeability and fractional volume. Kinetic modelling of cerebral D-glucose transport and metabolism is discussed in Chapter 8.

In DGE MRI, most studies have relied on visual assessment and calculation of AUC maps as described in Paper II. Based on the idea of temporal enhancement patters reflecting underlying physiology, we developed a curve shape-based analysis method for DGE MRI as reported in Paper III. The purpose was to introduce a more informative post-processing method for DGE MRI, but without the need for assumptions or ROI-based assessment. DGE and DCE MRI data were acquired in patients with brain tumour at 7 T, and the tissue response curve in each voxel was classified as one out of seven curve types, creating a visual representation of different curve shapes, referred to as a curve map. The generalized curve types and the corresponding colours and numbers are shown in Figure 7.2, together with an example of a DGE curve map.
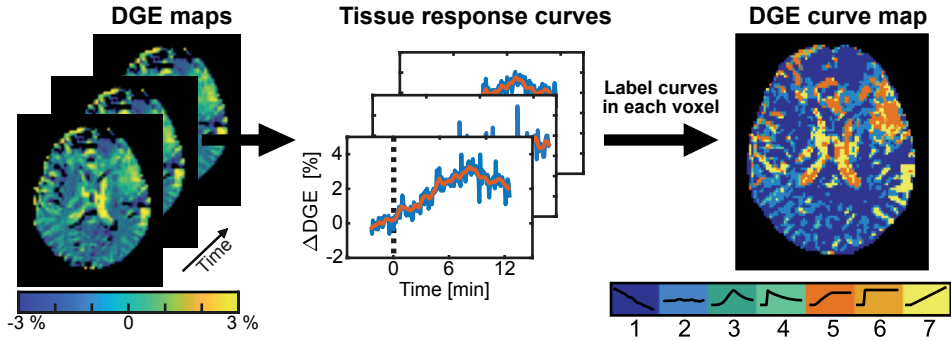
**DGE maps** · **Tissue response curves** · Label curves in each voxel · **DGE curve map**

**Figure 7.2.** Illustration showing the principle of the post-processing approach introduced in Paper III. The tissue response curve in each voxel was color-coded by classifying it as one out of seven predefined curve types, shown in the bottom right. Figure adapted from Paper III, published by Wiley and licensed under CC BY 4.0.

In a DCE MRI study of patients with recurring glioma, Lavini et al. performed curve shape analysis using seven curve types, and compared the results to kinetic modelling parameters (145). The authors showed that their equivalent to our curve type 6 was associated with high $K_{ep}$ (reflux rate constant of gadolinium from the EES back into plasma) and low $V_e$ (EES fractional volume). The equivalent to our curve type 3 corresponded, in general, to high $V_e$ and $V_i$ (plasma fractional volume), and intermediate $K_{ep}$. The equivalent to our curve type 5 was associated with high $V_e$ and low $K_{ep}$. The volume transfer constant for contrast agent from blood plasma to the EES ($K^{trans}$) was similar across all their investigated curve types. Comparison to kinetic modelling parameters was not possible in Paper III, due to the lack of a kinetic model for DGE MRI at the time. However, such a comparison would be a logical next step after the introduction of our kinetic model for DGE MRI, presented in Chapter 8. It should also be emphasized that since the kinetics differ between gadolinium and D-glucose, Lavini's results are not directly translatable to the results given in Paper III. As exemplified in one patient in Figure 7.3, the most common DCE curve type in tumour observed in Paper III was type 5, which would indicate a large volume of EES. Based on this, it seems reasonable to assume that the higher DGE MRI signal in the tumours seen in Paper III reflects a disrupted BBB, and thus accumulation of D-glucose in the EES, as well as a larger EES volume, giving a higher DGE MRI signal due to the lower pH in tumour EES.
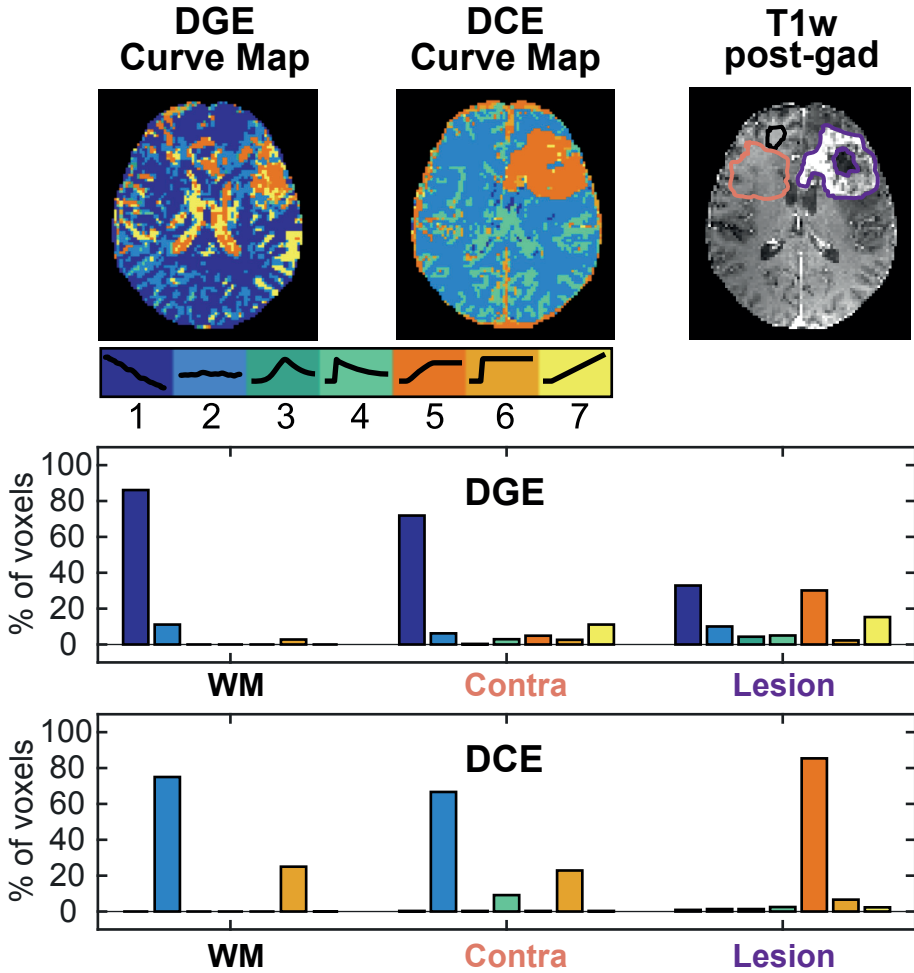
**Figure 7.3**. Curve maps and relative frequency of curve types in white matter (WM) contralateral tissue (Contra) and gadolinium-enhancing part of the lesion. Top row: DGE and DCE curve maps of Patient 1 in Paper III, shown together with a $T_1$w post-gadolinium (post-gad) image, showing the ROIs used in the bar plots (centre and bottom). The seven curve types and their corresponding colors are shown below the curve maps. Centre and bottom rows: Bar plots showing the relative frequency of curve types within each ROI. Figure adapted from Paper III, published by Wiley and licensed under CC BY 4.0.

# 8. Quantification of glucose uptake

Dynamic imaging methods, such as DGE MRI, allow for assessment of the signal change over time caused by administration of a contrast agent (here D-glucose or other sugars). The measured tissue response curve is a temporally varying superposition of signal contributions from sugars in different tissue compartments or different metabolic stages, and to retrieve the desired physiological information, e.g. D-glucose delivery, transport and metabolism, the signal contributions from different tissue compartments must be isolated. One way to do this is by kinetic modelling. The physiological system is incredibly complex and needs to be simplified, for example using a compartment model as shown previously in Figure 3.1. Too detailed a description of glucose transport and metabolism would result in a model with a large number of unknowns, implying a close to impossible task when it comes to quantifying the kinetic parameters from a single response curve.

In contrast to many other kinetic imaging techniques, DGE MRI offers a possibility to deduce information from the EES separately due to the different exchange properties between compartments, as discussed in previous chapters. However, quantification of DGE MRI is not straightforward, as robust fitting requires sufficient temporal resolution and SNR. As we have seen in previous chapters and in Papers I and II, the glucoCEST effect is small, and the curves can be contaminated by motion artefacts, $B_0$-shifts and PVEs. In addition, conversion from signal to concentration, the involvement of many unknown parameters, and the need for measurement of individual AIFs further complicate the situation, as described in Paper III. In Paper IV, we introduce a kinetic model for DGE MRI by utilizing Michaelis-Menten (MM) kinetics and expanding and adapting previous compartment models.

## 8.1 Assessment of glucose transport and metabolism

Quantification of glucose transport and metabolism aims to provide information on cerebral function, tumour aggressiveness, tissue viability, among other things, and PET using ^{18}F-FDG is widely utilized in this context. MRS of non-radioactive isotopes such as ^{13}C and ^{2}H can also be used to assess these processes, but is not yet used in the clinic. In Sections 8.1.1 and 8.1.2, a brief background of MM kinetics and compartment

models will be outlined, after which our proposed kinetic model for DGE MRI will be introduced in Section 8.2.

## 8.1.1 Michaelis-Menten kinetics

As mentioned in Chapter 3, the glucose transport into the brain is facilitated and saturable (148), and the amount of transporters does not change during the experiment. Glucose transport can thus be modelled according to Michaelis-Menten kinetics (149). The MM model describes enzyme kinetics by relating the reaction velocity $v$ (the rate at which a product P is formed) to the substrate concentration S. The schematic representation of this process is:

$$E + S \underset{k_2}{\overset{k_1}{\rightleftarrows}} ES \overset{k_3}{\rightarrow} E + P, \qquad \text{(Eq. 8.1)}$$

where in the first step (left), the enzyme E forms a complex with the total substrate S, creating an enzyme-substrate complex ES. For the single enzyme-catalysed reaction in Eq. 8.1, the model is defined by three rate constants $k_i$ (i = 1,2,3): $k_1$, describing the rate of formation of the ES complex, $k_2$, describing the rate of the backward reaction i.e. the dissociation of ES back to E and S, and $k_3$, describing the rate of conversion of ES to E and P. Under the assumption that the enzyme concentration [E] is much smaller than the substrate concentration [S], the rate of product formation is given by the MM equation:

$$v = \frac{d[P]}{dt} = \frac{V_{max}[S]}{K_M + [S]}, \qquad \text{(Eq. 8.2)}$$

in which $V_{max}$ is the asymptotic maximum rate when all of the enzyme is complexed to the substrate, and $K_M$ is the so-called Michaelis-Menten constant, representing the substrate concentration at which the reaction rate is half of $V_{max}$.

In modelling of D-glucose transport, the rates refer to the transport (flux) over a barrier. The MM-equation for one-directional glucose transport over a single membrane is (150):

$$J = \frac{T_{max} \, [\text{D-glucose}]}{K_T + [\text{D-glucose}]}, \qquad \text{(Eq. 8.3)}$$

where $J$ represents the unidirectional flux (transport rate) over the barrier in μmol/g/min, $T_{max}$ is the maximum transport rate in μmol/g/min, [D-glucose] is the glucose concentration in mM, and $K_T$ is the half-saturation constant in mM (i.e., the concentration at which the transport rate is half of $T_{max}$).

MM kinetics can thus be used to estimate both glucose transport and metabolism, and thus also for prediction of brain glucose concentration from blood glucose concentration (94, 101). The flux over the BBB as a function of plasma glucose concentration, and the phosphorylation rate as a function of brain tissue concentration are illustrated with MM saturation plots in Figure 8.1. These curves were calculated using Equations 8.3 and 8.2, respectively, and the inserted values were $T_{max}$ = 1.0 µmol/g/min, $K_T$ = 5.0 mM, approximated from results obtained in $^{13}$C NMR (101) and $^1$H NMR (94, 151) studies of D-glucose in humans. For the MM constants for hexokinase, $K_M$ = 50 µM, $V_{max}$ = 0.3 µmol/g/min, the enzyme literature was used (152, 153).
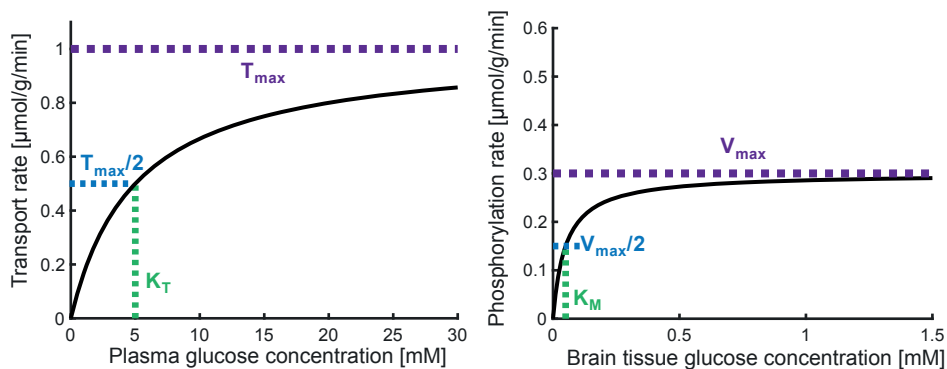


**Figure 8.1.** Simulation of the Michaelis-Menten saturation curves for the rate of uni-directional transport over the BBB (left) and the rate of D-glucose phosphorylation (right), calculated using Eqns. [8.3] and [8.2], respectively, together with realistic MM parameters from the literature.

From Figure 8.1, it becomes clear that the transport over the BBB does not become saturated at physiological plasma glucose levels. However, the phosphorylation rate is close to saturated already at baseline brain tissue glucose concentrations (≈ 1 mM (95, 151, 154)), allowing for the use of the assumption that $CMR_{glc}$ is constant at euglycemia and above. Figure 8.1 illustrates that D-glucose phosphorylation in the cells is the rate-limiting step in normal brain tissue rather than D-glucose transport over the BBB.

As we have just seen, MM kinetics can be used to describe both transport across the BBB and across cell membranes, as well as phosphorylation (metabolism) of D-glucose.

## 8.1.2 Compartment models

The most common kinetic model used for D-glucose transport and metabolism in vivo is a 2-compartment exchange model (vascular and extravascular tissue) combined with

MM kinetics principles (Fig. 8.2a). It was used first in the autoradiography (111, 155, 156) and PET literature (157) and later in the $^{13}$C, $^{2}$H and $^{1}$H MRS literature (93-95, 101, 151). Recently, it was also employed in glucoCESL MRI (158), including the addition of a diffusion term to account for BBB breakdown in tumours. Thus, all these methods assume two exchanging compartments, one blood compartment representing delivery of glucose, and one brain tissue compartment, representing a mixture of extravascular extracellular and intracellular glucose, in which D-glucose is metabolized. This is practical, because PET and MRS cannot distinguish EES from cellular components in the voxel. While the 2-compartment model might be applicable to DGE MRI in healthy tissue, it is unlikely to work in tumour tissue. This is because, in the case of BBB breakdown, the concentration in the EES equilibrates with the blood compartment, but not with the intracellular compartment. In addition, the pH in the EES of tumours is reduced, leading to a reduced -OH exchange rate and thus an increased glucoCEST signal contribution from this compartment. In Paper IV, we revised the model to be able to account for EES concentration and pH.

The goal of modelling in general is to estimate physiologically relevant parameters that are difficult to assess directly from the experiment. To achieve this, the tissue of interest must be simplified for example using a compartment model, as introduced in Figure 3.1 and in Figure 8.2. The arrows in Figure 8.2 denote rate constants, representing the exchange between the compartments.
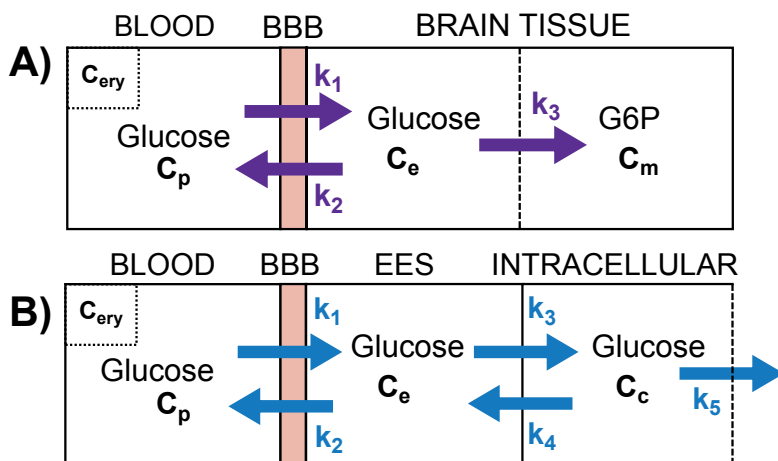


**Figure 8.2**. Example of compartment models. (A) 2-compartment model where the EES and the intracellular space are one compartment (dashed line indicate no compartment barrier); (B) 3-compartment model where the EES and the intracellular space are separate compartments (solid line indicates compartment barrier). $C_p$ plasma concentration; $C_e$ concentration in the extravascular extracellular space (EES); $C_c$ intracellular concentration; $C_m$ concentration of phosphorylated glucose (G6P); $k_1$ to $k_5$ are rate constants, describing the transfer between the compartments. The blood compartment contains plasma (p) and erythrocytes (ery).

The concentration change over time within the compartments can be described by a set of differential equations. One equation for each unknown quantity is required, so by studying these equations it becomes clear why further simplifications may sometimes be needed. The system of differential equations describing the 3-compartment model in Figure 8.2b is:

$$\frac{dC_p(t)}{dt} = -k_1 C_p(t) + k_2 C_e(t) \tag{Eq 8.4a}$$

$$\frac{dC_e(t)}{dt} = k_1 C_p(t) - k_2 C_e(t) - k_3 C_e(t) + k_4 C_c(t) \tag{Eq 8.4b}$$

$$\frac{dC_c(t)}{dt} = k_3 C_e(t) - k_4 C_c(t) - k_5 C_c(t). \tag{Eq 8.4c}$$

Importantly, it has to be realized that the originally defined rate constants in relation to the MM kinetics described in Eqns. 8.1 and 8.2 describe exchange between metabolites in water solution, and the concentrations are in mM, i.e. in µmol/mL water. This approach is not really applicable to tissue, where the rates would need to reflect amount of glucose taken up or metabolized per volume or mass of tissue, and concentrations are generally given in µmol/mL tissue or µmol/g tissue. In addition, different types of tissues, for example, GM versus WM, show different metabolic rates of D-glucose ($CMR_{glc}$). In response, the body delivers different amounts of D-glucose (flow-metabolism coupling for oxidative metabolism), but the MM constants for transport over the BBB would have to be the same. To account for this, the PET literature has used a volume transfer constant $K_1$ (units of mL blood/g tissue/min) instead of the rate constant $k_1$.

Finally, it is important to comment on MRS. In proton MRS methods, the concentration of tissue metabolites is reported in millimolar because they are determined using tissue water as a reference. In that approach it is therefore not needed to have a volume transfer constant. However, the situation is not totally trivial, since the metabolites are also compartmentalized, while the water signal origins from the whole voxel. Thus, when reporting the brain tissue concentration, an averaging is done for blood, EES and cellular concentrations of D-glucose based on the volume fractions of these components in tissue, which may not be the water volume fractions as the water content differs for these compartments.

## 8.2 Kinetic models for DGE MRI

As mentioned above, there is currently one paper (Dickie et al. (158)) describing glucose uptake in tissue using the common 2-compartment model for DGE MRI. In Paper IV, we have extended this to the model in Fig. 8.3, containing three tissue compartments (separated by solid lines to indicate facilitated transport) and two metabolic steps, namely D-glucose phosphorylation by hexokinase and a single step for the further breakdown to pyruvate, which is in equilibrium with lactate and substrate for the TCA cycle in healthy cells, while lactate is the end product in tumour cells. In addition, for the non-tracer-level concentrations of D-glucose are accounted for by using a reversible facilitated transport model (95, 151, 154, 159).
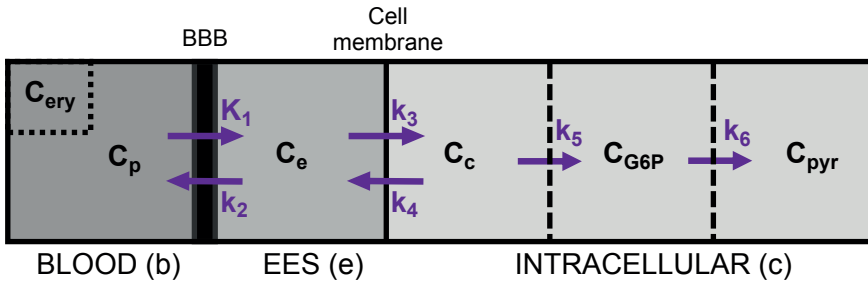


**Figure 8.3.** Schematic illustration of a 3-compartment model describing facilitated transport in two reversible steps: between blood (containing plasma (p) and erythrocytes (ery)), and the EES (e), and between the EES and the cell (c). The two irreversible metabolic steps accounting for phosphorylation of D-glucose to G-6P, and the metabolism to pyruvate are also included. $K_1$ is a volume transfer constant, while $k_2$ to $k_5$ are rate constants, describing the transfer between compartments.

The differential equations describing the glucose fluxes [µmol/g/min] between the compartments depicted in Figure 8.3 are:

$$\frac{dC_p(t)}{d_{tissue}dt} = -K_{1,tissue}(t)C_p(t) + k_2(t)C_e(t), \qquad \text{(Eq. 8.5a)}$$

$$\frac{dC_e(t)}{d_{tissue}dt} = K_{1,tissue}(t)C_p(t) - k_2(t)C_e(t) - k_3(t)C_e(t) + k_4(t)C_c(t), \qquad \text{(Eq. 8.5b)}$$

$$\frac{dC_c(t)}{d_{tissue}dt} = k_3(t)C_e(t) - k_4(t)C_c(t) - k_5(t)C_c(t), \qquad \text{(Eq. 8.5c)}$$

$$\frac{dC_{G6P}(t)}{d_{tissue}dt} = k_5(t)C_c(t) - k_6(t)C_{G6P}(t), \qquad \text{(Eq. 8.5d)}$$

in which $K_1 = k_1/\rho_b^{V/V}$, where $\rho_b^{V/V}$ is a volume/volume water content correction (mL water/mL blood), $d_{tissue}$ is the tissue density (g tissue/mL tissue), and $k_i$ are the rate constants (mL water/g tissue/min) described by Eqns. 8.6a-8.6.b. The rate constants $k_1$ and $k_2$ represent transport (influx and efflux, respectively) over the BBB. Similarly, $k_3$ and $k_4$ represent transport (influx and efflux, respectively) over the cell membrane, $k_5$ represents phosphorylation by hexokinase (HK) and $k_6$ represents residual glycolysis. Importantly, to properly account for the non-tracer character of D-glucose in MR experiments (concentrations in mM), Eqns. 8.6a-8.6b are based on the reversible transport model of Cunningham et al. (95, 151, 154, 159) . The forward and reverse rate constants for transport over the BBB or cell membrane are then equivalent, as D-glucose molecules on both sides of the membrane compete for the same receptors.

$$k_1(t) = k_2(t) = \frac{T_{max}^{BBB}}{C_p(t)/\rho_p^{V/V} + C_e(t) + K_T}, \quad \text{(Eq. 8.6a)}$$

$$k_3(t) = k_4(t) = \frac{T_{max}^{cell\ membrane}}{C_e(t) + C_c(t) + K_T}, \quad \text{(Eq. 8.6b)}$$

$$k_5(t) = \frac{V_{max}^{HK}}{C_c(t) + K_M^{HK}}, \quad \text{(Eq. 8.6c)}$$

$$k_6(t) = \frac{V_{max}^{glyc}}{C_{G6P}(t) + K_M^{glyc}}, \quad \text{(Eq. 8.6d)}$$

where $glyc$ represents glycolysis to pyruvate.

As a first validation of the model, we used existing MRS data from Shestov et al. (151), who measured plasma concentrations and concentrations of D-glucose in GM when raising the plasma levels from euglycemia (~ 5 mM) to hyperglycaemia (16-18 mM). Dr. Öz (last author of Ref. (151)) kindly provided the original data. Using the plasma concentration from Shestov et al. as input function $C_p(t)$, the compartmental glucose concentrations $C_e(t)$, $C_c(t)$ and $C_{G6P}(t)$ were calculated stepwise by numerically solving Eqns. 8.5a-8.5d. The corresponding brain concentrations were determined using:

$$C_{brain,tissue} = [f_{b,tissue}C_p + f_{e,tissue}\rho_e^{V/V}C_e$$
$$+ f_{c,tissue}\rho_{tissue-cell}^{V/V}(C_c + C_{G6P})]/\rho_{tissue-whole}^{V/V}, \quad \text{(Eq. 8.7)}$$

$\rho^{V/V}$ is the volume/volume water content (mL water/mL tissue) correction for each compartment and $f$ is the fractional volume of a compartment. Predefined ranges of

MM parameters $T_{max}$, $k_T$, $V_{max}$, $k_M$ were used to simulate a large set of possible $C_{brain,GM}$ curves. The agreement of these curves with the experimental GM concentration curves were compared and the root mean squared error was assessed.

The MM parameters retrieved from the best fit to the MRS brain concentration curve were then used to calculate $C_e(t)$, $C_c(t)$ and $C_{G6P}(t)$ for different tissue compartments (WM and GM). Tumour was simulated by adjusting the MM parameters for BBB transport to represent BBB breakdown. Finally, these concentration curves were used to simulate the signal changes expected in a DGE MRI experiment using the Bloch-McConnell equations for each tissue compartment. The DGE signals in tumour EES and tumour cell were simulated separately to account for the different exchange rates due to different pH in tumour EES and cell. The total tumour DGE signal was then calculated from Eq 8.7 by substituting signal for concentration.

The model was validated qualitatively through comparison with experimental DGE data. Blood glucose levels from three glioblastoma patients included in Paper III were used as input function to simulate concentration curves in GM, WM, and tumor. DGE MRI response curves in tumour, blood, GM and WM were then simulated as described above. An example of a measured input function, simulated concentration curves in different tissue compartments, and simulated as well as experimentally measured DGE signals in one patient are shown in Figure 8.4. Images of this patient is shown in Figures 7.2 and 7.3. The results indicate that in tumour, the EES, because of its concentration equal to plasma and lower pH, and thus slower exchange rate, is the dominating DGE MRI signal contributor.

On a final note, the proposed 3-compartment model can be adapted for other sugars than D-glucose by adjusting the MM parameters to account for the different transport kinetics of other sugars such as 2-DG, 3-OMG and L-glucose. A first demonstration of simulations of D-glucose, 2-DG, 3-OMG and L-glucose concentrations in different compartments was shown in Figure 5.1.
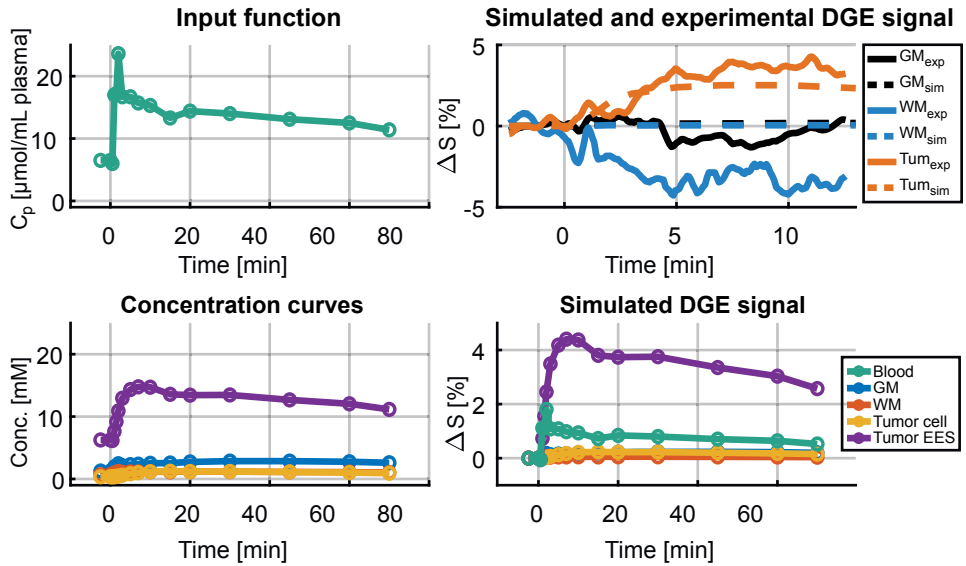
**Figure 8.4.** Experimental and simulated concentration and DGE signal ($\Delta S$) curves in one glioblastoma patient (images shown in Figures 7.2 and 7.3). The measured plasma D-glucose concentration $C_p$ (top left), simulated concentrations in GM, WM, tumour cell and tumour EES (bottom left), and corresponding simulated DGE signal contributions corrected for compartmental fractions are shown to the right, bottom row. Simulated and experimental DGE MRI signals are shown in the top right panel.

# 9. Conclusions and future aspects

The work presented in this thesis aimed at development and application of DGE MRI in humans, by implementation and optimization of imaging as well as post-processing methods.

In the study reported in Paper I, DGE MRI was applied to healthy volunteers scanned at 7 T. The main conclusion of Paper I was that both AIFs and tissue response curves can be obtained using DGE MRI at 7 T, and that DGE AIFs were correlated to the change in venous blood glucose level. The shape and magnitude of the tissue response curves differed between volunteers, and these variations were attributed to individual insulin responses. Another conclusion of this study was that the interpretation of the tissue response curves is complicated by partial volume effects and the low D-glucose concentration in healthy brain tissue. Normal tissue perfusion parameters might therefore be difficult to assess, but this could, on the other hand, enable separation of tumour from normal tissue responses.

Paper II describes a step towards clinical DGE imaging by optimizing a DGE MRI protocol at 3 T. The conclusion of Paper II was that it is possible to measure DGE AIFs in healthy individuals at 3 T, but that the measured DGE signal change depends not only on blood glucose concentration change but may also depend on motion-induced $B_0$ artefacts. An additional conclusion was that a longer infusion duration (e.g. 3-4 minutes) should be recommended for glucoCEST experiments, since it can minimize the side effects of the D-glucose infusion while still producing sufficient change in blood glucose level. It was also demonstrated that the 1.2 ppm saturation frequency offset, typically used at higher field strengths (7 T and above), is not optimal for DGE MRI at 3 T due to the increased coalescence of the glucose resonances with water, leading to increased sensitivity to motion-induced $B_0$ shifts.

Future aspects related to the studies in Papers I and II include further development and optimization of the DGE image acquisition protocol, for example by saturation at several frequency offsets, the inclusion of dynamic $B_0$-correction and implementation of more sophisticated motion correction algorithms.

In Paper III, a more comprehensive analysis of DGE images in patients with brain tumours scanned at 7 T was proposed. The introduced post-processing method had potential to facilitate tumour detection and characterization. The comparison of DGE and DCE MRI showed that in some cases, the DGE images had enhancement in

regions that were not enhanced in the images obtained from DCE MRI. This was attributed to the different uptake kinetics of D-glucose and gadolinium. The DGE images also showed a slower signal increase than the images from DCE MRI, likely due to the longer D-glucose infusion duration and thus delivery, and possibly metabolism. In future work, the curve map approach could be further optimized for DGE MRI, either simplified, for example, by reducing the number of curve types, or refined, for example, by including different colour intensities for different magnitudes or slopes.

In the study described in Paper IV a model for characterization of D-glucose transport and metabolism was developed. The simulated DGE signals were found to be similar to the experimental curves shown in Papers I –III. For completeness, the model introduced in Paper IV should in the future be expanded by inclusion of a CSF compartment, and by separation of the blood compartment into arterial and venous components. Also, the CBF range used for the parameter determination in the model was based on recent values from the PET literature for adults. This range can be extended to include higher CBF values, such as those observed in paediatric populations.

Future applications of the combination of the methods used in Papers III and IV include comparison between curve maps and physiological parameter maps yielded by the kinetic analysis. The simulation of concentration and DGE curves described in Paper IV could probably be used to further improve the curve classification algorithm introduced in Paper III, by creating realistic curves to be used in the training of the model. The ability of utilizing the curve classification algorithm to obtain AIFs should also be explored as the use of image-based AIFs is necessary if blood glucose levels are not available.

A mutual limitation among all the studies presented in Papers I – IV is the small number of healthy volunteers or patients enrolled in each study. Therefore, future DGE MRI studies should include larger cohorts, especially patients with brain tumours.

The aggregated conclusions of the work included in this thesis are that DGE MRI has potential for tumour detection in humans and that information on glucose delivery, transport, and metabolism can be obtained. The technique is associated with challenges, especially at lower field strengths where the glucoCEST signal in vivo is small. However, the proposed post-processing methods may enable human DGE MRI to be fully utilized when experimental CEST acquisition methods become sufficiently improved.

# Acknowledgements

*"My brain hurt like a warehouse, it had no room to spare*
*I had to cram so many things to store everything in there*
*And all the fat, skinny people*
*And all the tall, short people*
*And all the nobody people*
*And all the somebody people*
*I never thought I'd need so many people"*
**Five Years – David Bowie (1972)**

When I am writing this, it is approximately five years since I started my journey with glucoCEST in the form of a master thesis. It is perhaps still unclear whether the world will end or not once these five years have passed, but it is for sure the end of an era. Many people have been of importance to me and my work, and I would like to spend a few pages to express my gratitude to some of them.

First of all, I want to thank my supervisor and role model Linda Knutsson for supporting me scientifically as well as personally. I could fill this whole page solely with praise for you. You are always available, you always have a solution, and you have basically taught me all I need to know about everything. So, thank you, I can only hope that you will remain my personal advisor after my dissertation.

I also want to thank my co-supervisors. Ronnie Wirestam, you impressed me from the first overhead sheet in the undergraduate education. While I must admit that your correctness scared me at first, this is also something I admire and that makes me trust you one hundred percent. Gunther Helms, your knowledge, anecdotes and sometimes also criticism have helped turning me into a better scientist.

Peter van Zijl, thank you for your patience and for giving me so much time and support. It has truly been amazing to work this close together and to have you in my corner.

I want to express my gratitude to my co-authors in Lund: Pia Sundgren, Karin Markenroth-Bloch, Anna Rydhög, Patrick Lehmann, Mads Andersen and Johan

Bengzon, and to my collaborators in Baltimore, particularly Nirbhay Yadav and Xiang Xu. I know I can always rely on you.

I want to thank all members of the Lund MR physics group. Each of you have influenced me in one way or another. I especially want to mention Jimmy Lätt for inspiring me to go in the MR direction, and Anna Rydhög for letting me tail you during my first shaky steps into the MR world. I am also grateful to the radiographers at BoF in Lund who helped run our experiments.

Thanks to all my colleagues at Medical Radiation Physics in Lund, you have all contributed to create an environment that now feels like home. The PhD student group deserves to be mentioned separately. You inspire me and have all helped create the feeling that we are in this together. A special shout-out to Annika Mannerberg for all our conversations, with our office door open or closed. Thanks also to Patrick Lehmann, for being my professional other half. We have had so much fun and learned so much together.

I want to acknowledge all the volunteers and patients that participated in our studies. Obviously, this work would not have been possible without your brains either.

I want to thank my parents for providing me with a creative mind. Mamma, thank you for believing in me regardless of what weird job, hobby or project that I throw myself into, and for teaching me that sometimes the impossible is possible, if you just have the guts to try it. Pappa, thank you for awakening my curiosity and my interest in science. It hurts me infinitely that you never get to see the results of my work. Thanks to my sisters Fanny and Emma for all your love and support, especially during the summer of 2020 when our world suddenly fell apart.

I am grateful to all my friends for distracting me with bubbel, music and singing, whenever I need it (you probably know better than me whenever that is). Special thanks to Cissi and Mattan for all the encouragement, breakfasts and dinners you provided during this latest intense period.

Finally, a most sincere thank you to Lisa for always having my back. You have the ability not only to accept, but also to help structure my sometimes rather confused existence. I also want to thank our cats for having soft fur, and our house and garden for being everything I ever wished for.

And yes, the earth is probably really dying, and just as in "Five Years", it feels as if the apocalypse has been luring around the corner more than once lately. Nevertheless, thanks to all these people, and everyone else that I forgot to mention, this thesis work was finally finished. And with your support, I wouldn't hesitate to spend another five years to do it all over again.

# References

1.  Marckmann P, Skov L, Rossen K, Dupont A, Damholt MB, Heaf JG, et al. Nephrogenic systemic fibrosis: suspected causative role of gadodiamide used for contrast-enhanced magnetic resonance imaging. J Am Soc Nephrol. 2006;17(9):2359-62.

2.  Thomsen H, Morcos S, Almén T, Bellin M, Bertolotto M, Bongartz G, et al. Nephrogenic systemic fibrosis and gadolinium-based contrast media: updated ESUR Contrast Medium Safety Committee guidelines. Eur Radiol. 2013;23(2):307-18.

3.  Errante Y, Cirimele V, Mallio CA, Di Lazzaro V, Zobel BB, Quattrocchi CC. Progressive increase of T1 signal intensity of the dentate nucleus on unenhanced magnetic resonance images is associated with cumulative doses of intravenously administered gadodiamide in patients with normal renal function, suggesting dechelation. Invest Radiol. 2014;49(10):685-90.

4.  Kanda T, Ishii K, Kawaguchi H, Kitajima K, Takenaka D. High signal intensity in the dentate nucleus and globus pallidus on unenhanced T1-weighted MR images: relationship with increasing cumulative dose of a gadolinium-based contrast material. Radiology. 2014;270(3):834-41.

5.  Robert P, Lehericy S, Grand S, Violas X, Fretellier N, Idee JM, et al. T1-weighted hypersignal in the deep cerebellar nuclei after repeated administrations of gadolinium-based contrast agents in healthy rats: difference between linear and macrocyclic agents. Invest Radiol. 2015;50(8):473-80.

6.  McDonald RJ, McDonald JS, Kallmes DF, Jentoft ME, Murray DL, Thielen KR, et al. Intracranial gadolinium deposition after contrast-enhanced MR imaging. Radiology. 2015;275(3):772-82.

7.  Lord M, Chettle D, Grafe J, Noseworthy M, McNeill F. Observed deposition of gadolinium in bone using a new noninvasive in vivo biomedical device: results of a small pilot feasibility study. Radiology. 2018;287(1):96-103.

8.  Scott JN, Brasher PM, Sevick RJ, Rewcastle NB, Forsyth PA. How often are nonenhancing supratentorial gliomas malignant? A population study. Neurology. 2002;59(6):947-9.

9.  Upadhyay N, Waldman AD. Conventional MRI evaluation of gliomas. Br J Radiol. 2011;84 Spec No 2(Spec Iss 2):S107-11.

10. Kumar AJ, Leeds NE, Fuller GN, van Tassel P, Maor MH, Sawaya RE, et al. Malignant gliomas: MR imaging spectrum of radiation therapy- and chemotherapy-induced necrosis of the brain after treatment. Radiology. 2000;217(2):377-84.

11. Rock JP, Hearshen D, Scarpace L, Croteau D, Gutierrez J, Fisher JL, et al. Correlations between magnetic resonance spectroscopy and image-guided histopathology, with special attention to radiation necrosis. Neurosurg. 2002;51(4):912-9.

12. Butowski NA, Sneed PK, Chang S. Diagnosis and treatment of recurrent high-grade astrocytoma. J Clin Onc. 2006;24(8):1273-80.

13. Brandsma D, Stalpers L, Taal W, Sminia P, van den Bent MJ. Clinical features, mechanisms, and management of pseudoprogression in malignant gliomas. Lancet Oncol. 2008;9(5):453-61.

14. Rogowska J, Olkowska E, Ratajczyk W, Wolska L. Gadolinium as a new emerging contaminant of aquatic environments. Environ Toxicol Chem. 2018;37(6):1523-34.

15. Inoue K, Fukushi M, Furukawa A, Sahoo SK, Veerasamy N, Ichimura K, et al. Impact on gadolinium anomaly in river waters in Tokyo related to the increased number of MRI devices in use. Mar Pollut Bull. 2020;154:111148.

16. Ward KM, Aletras AH, Balaban RS. A new class of contrast agents for MRI based on proton chemical exchange dependent saturation transfer (CEST). J Magn Reson. 2000;143(1):79-87.

17. Chan KW, McMahon MT, Kato Y, Liu G, Bulte JW, Bhujwalla ZM, et al. Natural D-glucose as a biodegradable MRI contrast agent for detecting cancer. Magn Reson Med. 2012;68(6):1764-73.

18. Walker-Samuel S, Ramasawmy R, Torrealdea F, Rega M, Rajkumar V, Johnson SP, et al. In vivo imaging of glucose uptake and metabolism in tumors. Nat Med. 2013;19(8):1067-72.

19. Jin T, Mehrens H, Hendrich KS, Kim SG. Mapping brain glucose uptake with chemical exchange-sensitive spin-lock magnetic resonance imaging. J Cereb Blood Flow Metab. 2014;34(8):1402-10.

20. Xu X, Yadav NN, Knutsson L, Hua J, Kalyani R, Hall E, et al. Dynamic glucose-enhanced (DGE) MRI: translation to human scanning and first results in glioma patients. Tomography. 2015;1(2):105-14.

21. Xu X, Chan KW, Knutsson L, Artemov D, Xu J, Liu G, et al. Dynamic glucose enhanced (DGE) MRI for combined imaging of blood-brain barrier break down and increased blood volume in brain cancer. Magn Reson Med. 2015;74(6):1556-63.

22. Paech D, Schuenke P, Koehler C, Windschuh J, Mundiyanapurath S, Bickelhaupt S, et al. T1ρ-weighted dynamic glucose-enhanced MR imaging in the human brain. Radiology. 2017;285(3):914-22.

23. Jin T, Mehrens H, Wang P, Kim SG. Glucose metabolism-weighted imaging with chemical exchange-sensitive MRI of 2-deoxyglucose (2DG) in brain: sensitivity and biological sources. Neuroimage. 2016;143:82-90.

24. Schuenke P, Paech D, Koehler C, Windschuh J, Bachert P, Ladd ME, et al. Fast and quantitative T1ρ-weighted dynamic glucose enhanced MRI. Sci Rep. 2017;7:42093.

25. Xu X, Sehgal AA, Yadav NN, Laterra J, Blair L, Blakeley J, et al. D-glucose weighted chemical exchange saturation transfer (glucoCEST)-based dynamic glucose enhanced (DGE) MRI at 3T: early experience in healthy volunteers and brain tumor patients. Magn Reson Med. 2020;84(1):247-62.

26. Herz K, Lindig T, Deshmane A, Schittenhelm J, Skardelly M, Bender B, et al. T1ρo-based dynamic glucose-enhanced (DGEρ) MRI at 3 T: method development and early clinical experience in the human brain. Magn Reson Med. 2019;82(5):1832-47.

27. Luo J, Abaci Turk E, Gagoski B, Copeland N, Zhou IY, Young V, et al. Preliminary evaluation of dynamic glucose enhanced MRI of the human placenta during glucose tolerance test. Quant Imaging Med Surg. 2019;9(10):1619-27.

28. Wang J, Weygand J, Hwang KP, Mohamed AS, Ding Y, Fuller CD, et al. Magnetic resonance imaging of glucose uptake and metabolism in patients with head and neck cancer. Sci Rep. 2016;6:30618.

29. Chen P, Shen Z, Wang Q, Zhang B, Zhuang Z, Lin J, et al. Reduced cerebral glucose uptake in an Alzheimer's rat model with glucose-weighted chemical exchange saturation transfer imaging. Front Aging Neurosci. 2021;13:618690.

30. Chen L, Wei Z, Chan KW, Li Y, Suchal K, Bi S, et al. D-Glucose uptake and clearance in the tauopathy Alzheimer's disease mouse brain detected by on-resonance variable delay multiple pulse MRI. J Cereb Blood Flow Metab. 2021;41(5):1013-25.

31. Huang J, van Zijl PCM, Han X, Dong CM, Cheng GWY, Tse KH, et al. Altered D-glucose in brain parenchyma and cerebrospinal fluid of early Alzheimer's disease detected by dynamic glucose-enhanced MRI. Sci Adv. 2020;6(20):eaba3884.

32. Zaiss M, Herz K, Deshmane A, Kim M, Golay X, Lindig T, et al. Possible artifacts in dynamic CEST MRI due to motion and field alterations. J Magn Reson. 2019;298:16-22.

33. Forsén S, Hoffman RA. Study of moderately rapid chemical exchange reactions by means of nuclear magnetic double resonance. J Chem Phys. 1963;39(11):2892-901.

34. Wolff SD, Balaban RS. NMR imaging of labile proton exchange. J Magn Reson. 1990;86(1):164-9.

35. Grad J, Bryant RG. Nuclear magnetic cross-relaxation spectroscopy. J Magn Reson. 1990;90(1):1-8.

36. van Zijl PCM, Lam WW, Xu J, Knutsson L, Stanisz GJ. Magnetization transfer contrast and chemical exchange saturation transfer MRI. Features and analysis of the field-dependent saturation spectrum. Neuroimage. 2018;168:222-41.

37. van Zijl PCM, Yadav NN. Chemical exchange saturation transfer (CEST): what is in a name and what isn't? Magn Reson Med. 2011;65(4):927-48.

38. McConnell H. Reaction rates by nuclear magnetic resonance. J Chem Phys. 1958;28(3):430-1.

39. van Zijl PCM, Sehgal AA. Proton chemical exchange saturation transfer (CEST) MRS and MRI. eMagRes. 2016;5(2):1307-32.

40. van Zijl PCM, Jones CK, Ren J, Malloy CR, Sherry AD. MRI detection of glycogen in vivo by using chemical exchange saturation transfer imaging (glycoCEST). Proc Natl Acad Sci U S A. 2007;104(11):4359-64.

41. Rooney WD, Johnson G, Li X, Cohen ER, Kim SG, Ugurbil K, et al. Magnetic field and tissue dependencies of human brain longitudinal $^1H_2O$ relaxation in vivo. Magn Reson Med. 2007;57(2):308-18.

42. Li W, Grgac K, Huang A, Yadav N, Qin Q, van Zijl PCM. Quantitative theory for the longitudinal relaxation time of blood water. Magn Reson Med. 2016;76(1):270-81.

43. Matthew JB, Richards FM. The pH dependence of hydrogen exchange in proteins. J Biol Chem. 1983;258(5):3039-44.

44. Zhou J, van Zijl PCM. Chemical exchange saturation transfer imaging and spectroscopy. Prog NMR Spectr. 2006;48(2-3):109-36.

45. Zhou J, Lal B, Wilson DA, Laterra J, van Zijl PC. Amide proton transfer (APT) contrast for imaging of brain tumors. Magn Reson Med. 2003;50(6):1120-6.

46. Zhou J, van Zijl PCM. Defining an acidosis-based ischemic penumbra from pH-weighted MRI. Transl Stroke Res. 2011;3(1):76-83.

47. Hua J, Jones CK, Blakeley J, Smith SA, van Zijl PCM, Zhou J. Quantitative description of the asymmetry in magnetization transfer effects around the water resonance in the human brain. Magn Reson Med. 2007;58(4):786-93.

48. Zaiss M, Jin T, Kim SG, Gochberg DF. Theory of chemical exchange saturation transfer MRI in the context of different magnetic fields. NMR Biomed. 2022;35(11):e4789.

49. Mueller S, Stirnberg R, Akbey S, Ehses P, Scheffler K, Stocker T, et al. Whole brain snapshot CEST at 3T using 3D-EPI: Aiming for speed, volume, and homogeneity. Magn Reson Med. 2020;84(5):2469-83.

50. Zhang Y, Heo HY, Jiang S, Lee DH, Bottomley PA, Zhou J. Highly accelerated chemical exchange saturation transfer (CEST) measurements with linear algebraic modeling. Magn Reson Med. 2016;76(1):136-44.

51. Heo HY, Zhang Y, Lee DH, Jiang S, Zhao X, Zhou J. Accelerating chemical exchange saturation transfer (CEST) MRI by combining compressed sensing and sensitivity encoding techniques. Magn Reson Med. 2017;77(2):779-86.

52. Zhang Y, Heo HY, Lee DH, Jiang S, Zhao X, Bottomley PA, et al. Chemical exchange saturation transfer (CEST) imaging with fast variably-accelerated sensitivity encoding (vSENSE). Magn Reson Med. 2017;77(6):2225-38.

53. She H, Greer JS, Zhang S, Li B, Keupp J, Madhuranthakam AJ, et al. Accelerating chemical exchange saturation transfer MRI with parallel blind compressed sensing. Magn Reson Med. 2019;81(1):504-13.

54. Heo H-Y, Xu X, Jiang S, Zhao Y, Keupp J, Redmond KJ, et al. Prospective acceleration of parallel RF transmission-based 3D chemical exchange saturation transfer imaging with compressed sensing. Magn Reson Med. 2019;82(5):1812-21.

55. Zaiss M, Ehses P, Scheffler K. Snapshot-CEST: optimizing spiral-centric-reordered gradient echo acquisition for fast and robust 3D CEST MRI at 9.4 T. NMR Biomed. 2018;31(4):e3879.

56. Varma G, Lenkinski RE, Vinogradov E. Keyhole chemical exchange saturation transfer. Magn Reson Med. 2012;68(4):1228-33.

57. Knutsson L, Xu X, van Zijl PCM, Chan KWY. Imaging of sugar-based contrast agents using their hydroxyl proton exchange properties. NMR Biomed. 2022:e4784.

58. Zhou J, Zaiss M, Knutsson L, Sun PZ, Ahn SS, Aime S, et al. Review and consensus recommendations on clinical APT-weighted imaging approaches at 3T: application to brain tumors. Magn Reson Med. 2022;88(2):546-74.

59. Jones CK, Schlosser MJ, van Zijl PCM, Pomper MG, Golay X, Zhou J. Amide proton transfer imaging of human brain tumors at 3T. Magn Reson Med. 2006;56(3):585-92.

60. Jiang S, Yu H, Wang X, Lu S, Li Y, Feng L, et al. Molecular MRI differentiation between primary central nervous system lymphomas and high-grade gliomas using endogenous protein-based amide proton transfer MR imaging at 3 Tesla. Eur Radiol. 2016;26(1):64-71.

61. Choi YS, Ahn SS, Lee S-K, Chang JH, Kang S-G, Kim SH, et al. Amide proton transfer imaging to discriminate between low- and high-grade gliomas: added value to apparent diffusion coefficient and relative cerebral blood volume. Eur Radiol. 2017;27(8):3181-9.

62. Su C, Liu C, Zhao L, Jiang J, Zhang J, Li S, et al. Amide proton transfer imaging allows detection of glioma grades and tumor proliferation: comparison with Ki-67 expression and proton MR spectroscopy imaging. AJNR Am J Neuroradiol. 2017;38(9):1702-9.

63. Bai Y, Lin Y, Zhang W, Kong L, Wang L, Zuo P, et al. Noninvasive amide proton transfer magnetic resonance imaging in evaluating the grading and cellularity of gliomas. Oncotarget. 2017;8(4):5834-42.

64. Zou T, Yu H, Jiang C, Wang X, Jiang S, Rui Q, et al. Differentiating the histologic grades of gliomas preoperatively using amide proton transfer-weighted (APTW) and intravoxel incoherent motion MRI. NMR Biomed. 2018;31(1):e3850.

65. Zhang J, Zhu W, Tain R, Zhou XJ, Cai K. Improved differentiation of low-grade and high-grade gliomas and detection of tumor proliferation using APT contrast fitted from Z-spectrum. Mol Imaging Biol. 2018;20(4):623-31.

66. Durmo F, Rydhög A, Testud F, Lätt J, Schmitt B, Rydelius A, et al. Assessment of amide proton transfer weighted (APTw) MRI for pre-surgical prediction of final diagnosis in gliomas. PLoS One. 2020;15(12):e0244003.

67. Paech D, Windschuh J, Oberhollenzer J, Dreher C, Sahm F, Meissner J-E, et al. Assessing the predictability of IDH mutation and MGMT methylation status in glioma patients using relaxation-compensated multipool CEST MRI at 7.0 T. Neuro Oncol. 2018;20(12):1661-71.

68. Xu Z, Ke C, Liu J, Xu S, Han L, Yang Y, et al. Diagnostic performance between MR amide proton transfer (APT) and diffusion kurtosis imaging (DKI) in glioma grading and IDH mutation status prediction at 3 T. Eur J Radiol. 2021;134:109466.

69. Jiang S, Zou T, Eberhart CG, Villalobos MAV, Heo H-Y, Zhang Y, et al. Predicting IDH mutation status in grade-II gliomas using amide proton transfer-weighted (APTw) MRI. Magn Reson Med. 2017;78(3):1100-9.

70. Jiang S, Rui Q, Wang Y, Heo H-Y, Zou T, Yu H, et al. Discriminating MGMT promoter methylation status in patients with glioblastoma employing amide proton transfer-weighted MRI metrics. Eur Radiol. 2018;28(5):2115-23.

71. Zhou J, Tryggestad E, Wen Z, Lal B, Zhou T, Grossman R, et al. Differentiation between glioma and radiation necrosis using molecular magnetic resonance imaging of endogenous proteins and peptides. Nat Med. 2011;17(1):130-4.

72. Park JE, Kim HS, Park KJ, Kim SJ, Kim JH, Smith SA. Pre- and posttreatment glioma: comparison of amide proton transfer imaging with MR spectroscopy for biomarkers of tumor proliferation. Radiology. 2016;278:514-23.

73. Park JE, Kim HS, Park SY, Jung SC, Kim JH, Heo HY. Identification of early response to anti-angiogenic therapy in recurrent glioblastoma: amide proton transfer-weighted and perfusion-weighted MRI compared with diffusion-weighted MRI. Radiology. 2020;295(2):397-406.

74. Ma B, Blakeley JO, Hong X, Zhang H, Jiang S, Blair L, et al. Applying amide proton transfer-weighted MRI to distinguish pseudoprogression from true progression in malignant gliomas. J Magn Reson Imaging. 2016;44(2):456-62.

75. Joo B, Han K, Ahn SS, Choi YS, Chang JH, Kang S-G, et al. Amide proton transfer imaging might predict survival and IDH mutation status in high-grade glioma. Eur Radiol. 2019;29(12):6643-52.

76. Regnery S, Adeberg S, Dreher C, Oberhollenzer J, Meissner J-E, Goerke S, et al. Chemical exchange saturation transfer MRI serves as predictor of early progression in glioblastoma patients. Oncotarget. 2018;9(47):28772-83.

77. Song G, Li C, Luo X, Zhao X, Zhang S, Zhang Y, et al. Evolution of cerebral ischemia assessed by amide proton transfer-weighted MRI. Front in Neurol. 2017;8:67.

78. Zhou J, Payen JF, Wilson DA, Traystman RJ, van Zijl PCM. Using the amide proton signals of intracellular proteins and peptides to detect pH effects in MRI. Nat Med. 2003;9(8):1085-90.

79. Mergenthaler P, Lindauer U, Dienel GA, Meisel A. Sugar for the brain: the role of glucose in physiological and pathological brain function. Trends Neurosci. 2013;36(10):587-97.

80. World-Health-Organization. Definition and diagnosis of diabetes mellitus and intermediate hyperglycemia: report of a WHO/IDF consultation. Geneva: WHO; 2006.

81. Dienel GA. Brain glucose metabolism: integration of energetics with function. Physiol Rev. 2019;99(1):949-1045.

82. Rasmussen P, Wyss Mt, Lundby C. Cerebral glucose and lactate consumption during cerebral activation by physical activity in humans. FASEB J. 2011;25(9):2865-73.

83. Hasselbalch SG, Holm S, Pedersen HS, Svarer C, Knudsen GM, Madsen PL, et al. The ^{18}F-fluorodeoxyglucose lumped constant determined in human brain from extraction fractions of ^{18}F-fluorodeoxyglucose and glucose. J Cereb Blood Flow Metab. 2001;21(8):995-1002.

84. Patching SG. Glucose transporters at the blood-brain barrier: function, regulation and gateways for drug delivery. Mol Neurobiol. 2017;54(2):1046-77.

85. Duelli R, Kuschinsky W. Brain glucose transporters: Relationship to local energy demand. News Physiol Sci. 2001;16:71-6.

86. Clyne AM. Endothelial response to glucose: dysfunction, metabolism, and transport. Biochem Soc Trans. 2021;49(1):313-25.

87. Bittner CX, Loaiza A, Ruminot I, Larenas V, Sotelo-Hitschfeld T, Gutierrez R, et al. High resolution measurement of the glycolytic rate. Front Neuroenergetics. 2010;2:26.

88. Leybaert L, De Bock M, Van Moorhem M, Decrock E, De Vuyst E. Neurobarrier coupling in the brain: adjusting glucose entry with demand. J Neurosci Res. 2007;85(15):3213-20.

89. Leybaert L. Neurobarrier coupling in the brain: a partner of neurovascular and neurometabolic coupling? J Cereb Blood Flow Metab. 2005;25(1):2-16.

90. Duarte JMN, Morgenthaler FD, Lei H, Poitry-Yamate C, Gruetter R. Steady-state brain glucose transport kinetics re-evaluated with a four-state conformational model. Front Neuroenergetics. 2009;12:1:6.

91. Hasselbalch SG, Knudsen GM, Capaldo B, Postiglione A, Paulson OB. Blood-brain barrier transport and brain metabolism of glucose during acute hyperglycemia in humans. J Clin Endocrinol Metab. 2001;86(5):1986–90.

92. Barros LF, Bittner CX, Loaiza A, Porras OH. A quantitative overview of glucose dynamics in the gliovascular unit. Glia. 2007;55(12):1222-37.

93. Van Zijl PCM, D. Davis, S. M. Eleff, C. T. W. Moonen, R. J. Parker, and J. M. Strong. Determination of cerebral glucose transport and metabolic kinetics by dynamic MR spectroscopy. Am J Physiol Endocrinol Metab 1997;273(6):E1216–E27.

94. Gruetter R, Novotny EJ, Boulware SD, Rothman DL, Shulman RG. ^{1}H NMR studies of glucose transport in the human brain. J Cereb Blood Flow Metab. 1996;16(3):427-38.

95. de Graaf RA, Pan JW, Telang F, Lee JH, Brown P, Novotny EJ, et al. Differentiation of glucose transport in human brain gray and white matter. J Cereb Blood Flow Metab. 2001;21(5):483-92.

96. Ganapathy V, Thangaraju M, Prasad PD. Nutrient transporters in cancer: relevance to Warburg hypothesis and beyond. Pharmacol Ther. 2009;121(1):29-40.

97. Marie SKN, Oba-Shinjo SM. Metabolism and brain cancer. Clinics (Sao Paolo). 2011;66(S1):33-43.

98. Warburg O. On the origin of cancer cells. Science. 1956;123(3191):309-14.

99.   Smith TA. Facilitative glucose transporter expression in human cancer tissue. Br J Biomed Sci 1999;56(4):285–92.

100.  Yamamoto T, Seino Y, Fukumoto H, Koh G, Yano H, Inagaki N, et al. Overexpression of facilitative glucose transporter genes in human cancer. Biochem Biophys Res Commun 1990;170(1):223-30.

101.  Gruetter R, Novotny EJ, Boulware SD, Rothman DL, Mason GF, Shulman GI, et al. Direct measurement of brain glucose concentrations in humans by $^{13}$C NMR spectroscopy. Proc Natl Acad Sci USA. 1992;89(3):1109–12.

102.  Zhang L, Su F, Buizer S, Kong X, Lee F, Day K, et al. A polymer-based ratiometric intracellular glucose sensor. Chem Commun (Camb). 2014;50(52):6920-2.

103.  Leen WG, Willemsen MA, Wevers RA, Verbeek MM. Cerebrospinal fluid glucose and lactate: age-specific reference values and implications for clinical practice. PLoS One. 2012;7(8):e42745.

104.  Koepsell H. Glucose transporters in brain in health and disease. Pflugers Arch. 2020;472(9):1299-343.

105.  Deane R, Segal MB. The transport of sugars across the perfused choroid plexus of the sheep. J Physiol. 1985;362:245-60.

106.  Zaiss M, Anemone A, Goerke S, Longo DL, Herz K, Pohmann R, et al. Quantification of hydroxyl exchange of D-Glucose at physiological conditions for optimization of glucoCEST MRI at 3, 7 and 9.4 Tesla. NMR Biomed. 2019;32(9):e4113.

107.  Hill JB, Cowart DS, Hill JB, Biber TUL, Huffines WD. Mutarotase and glucose anomers: I. The contribution of various organs to the in vivo mutarotation of exogenous glucose and the clearance of glucose anomers by the kidney of the anesthetized dog II. Mutarotase activity in chemically damaged glycosuric rat kidneys. Biochem Med. 1967;1(1):62-86.

108.  Gatenby RA, Gillies RJ. Why do cancers have high aerobic glycolysis? Nat Rev Cancer. 2004;4(11):891-9.

109.  Yadav NN, Xu J, Bar-Shir A, Qin Q, Chan KW, Grgac K, et al. Natural D-glucose as a biodegradable MRI relaxation agent. Magn Reson Med. 2014;72(3):823-8.

110.  Gore JC, Brown MS, Mizumoto CT, Armitage IM. Influence of glycogen on water proton relaxation times. Magn Reson Med. 1986;3(3):463-6.

111. Sokoloff L, Reivich M, Kennedy C, Des Rosiers MH, Patlak CS, Pettigrew KD, et al. The [$^{14}$C]-deoxyglucose method for the measurement of local cerebral glucose utilization: theory, procedure, and normal values in the conscious and anesthetized albino rat. J Neurochem. 1977;28(5):897-916.

112. Miller LP, Villeneuve JB, Braun LD, Oldendorf BA. Effect of pharmacological doses of 3-O-methyl-D-glucose and 2-deoxy-D-glucose on rat brain glucose and lactate. Stroke. 1986;17(5):957–61.

113. Nasrallah FA, Pages G, Kuchel PW, Golay X, Chuang KH. Imaging brain deoxyglucose uptake and metabolism by glucoCEST MRI. J Cereb Blood Flow Metab. 2013;33(8):1270-8.

114. Jin T, Iordanova B, Hitchens TK, Modo M, Wang P, Mehrens H, et al. Chemical exchange-sensitive spin-lock (CESL) MRI of glucose and analogs in brain tumors. Magn Reson Med. 2018;80(2):488-95.

115. Jay TM, Dienel GA, Cruz NF, Mori K, Nelson T, Sokoloff L. Metabolic stability of 3-O-methyl-D-glucose in brain and other tissues. J Neurochem. 1990;55(3):989-1000.

116. Rivlin M, Tsarfaty I, Navon G. Functional molecular imaging of tumors by chemical exchange saturation transfer MRI of 3-O-Methyl-D-glucose. Magn Reson Med. 2014;72(5):1375-80.

117. Sehgal AA, Li Y, Lal B, Yadav NN, Xu X, Xu J, et al. CEST MRI of 3-O-methyl-D-glucose uptake and accumulation in brain tumors. Magn Reson Med. 2019;81(3):1993-2000.

118. Jenkins AP, Menzies IS, Nukajam WS, Creamer B. The effect of ingested lactulose on absorption of L-rhamnose, D-xylose, and 3-O-methyl-D-glucose in subjects with ileostomies. Scand J Gastroenterol. 1994;29(9):820-5.

119. Sigalet DL, Martin GR, Meddings JB. 3-O methylglucose uptake as a marker of nutrient absorption and bowel length in pediatric patients. J Parenter Enteral Nutr. 2004;28(3):158-62.

120. Buhler I, Walter R, Reinhart WH. Influence of D- and L-glucose on erythrocytes and blood viscosity. Eur J Clin Invest. 2001;31(1):79-85.

121. Xu X, Xu J, Knutsson L, Liu J, Liu H, Li Y, et al. The effect of the mTOR inhibitor rapamycin on glucoCEST signal in a preclinical model of glioblastoma. Magn Reson Med. 2019;81(6):3798-807.

122. Eleftheriou A, Ravotto L, Wyss MT, Warnock G, Siebert A, Zaiss M, et al. Simultaneous dynamic glucose-enhanced (DGE) MRI and fiber photometry measurements of glucose in the healthy mouse brain. Neuroimage. 2023;265:119762.

123. Schuenke P, Koehler C, Korzowski A, Windschuh J, Bachert P, Ladd ME, et al. Adiabatically prepared spin-lock approach for T1ρ-based dynamic glucose enhanced MRI at ultrahigh fields. Magn Reson Med. 2017;78(1):215-25.

124. Boyd PS, Breitling J, Zimmermann F, Korzowski A, Zaiss M, Schuenke P, et al. Dynamic glucose-enhanced (DGE) MRI in the human brain at 7 T with reduced motion-induced artifacts based on quantitative R1ρ mapping. Magn Reson Med. 2020;84(1):182-91.

125. Lehmann PM, Seidemo A, Andersen M, Xu X, Li X, Yadav NN, et al. A numerical human brain phantom for dynamic glucose-enhanced (DGE) MRI: on the influence of head motion at 3T. Magn Reson Med. 2023;89(5):1871-87.

126. Stancanello J, Terreno E, Castelli DD, Cabella C, Uggeri F, Aime S. Development and validation of a smoothing-splines-based correction method for improving the analysis of CEST-MR images. Contrast Media Mol Imaging. 2008;3(4):136-49.

127. Sun PZ, Farrar CT, Sorensen AG. Correction for artifacts induced by B0 and B1 field inhomogeneities in pH-sensitive chemical exchange saturation transfer (CEST) imaging. Magn Reson Med. 2007;58(6):1207-15.

128. Kim M, Gillen J, Landman BA, Zhou J, van Zijl PCM. Water saturation shift referencing (WASSR) for chemical exchange saturation transfer (CEST) experiments. Magn Reson Med. 2009;61(6):1441-50.

129. Kim M, Torrealdea F, Adeleke S, Rega M, Evans V, Beeston T, et al. Challenges in glucoCEST MR body imaging at 3 Tesla. Quant Imaging Med Surg. 2019;9(10):1628-40.

130. Chen M, Porte D. The effect of rate and dose of glucose infusion on the acute insulin response in man. JCEM. 1976;42(6):1168-75.

131. Duarte JM, Gruetter R. Characterization of cerebral glucose dynamics in vivo with a four-state conformational model of transport at the blood-brain barrier. J Neurochem. 2012;121(3):396-406.

132. Perley MJ, Kipnis DM. Plasma insulin responses to oral and intravenous glucose: studies in normal and diabetic subjects. J Clin Invest. 1967;46(12):1954-62.

133. DeFronzo RA, Tobin JD, Andres R. Glucose clamp technique: a method for quantifying insulin secretion and resistance. Am J Physiol 1979;237(3):214-23.

134. Takahashi K, Nakamura H, Sato H, Matsuda H, Takada K, Tsuji T. Four plasma glucose and insulin responses to a 75 g OGTT in healthy young Japanese women. J Diabetes Res. 2018;2018:5742497.

135. Hayashi T, Boyko EJ, Sato KK, McNeely MJ, Leonetti DL, Kahn SE, et al. Patterns of insulin concentration during the OGTT predict the risk of type 2 diabetes in Japanese Americans. Diabetes Care. 2013;36(5):1229-35.

136. Bender B, Herz K, Deshmane A, Richter V, Tabatabai G, Schittenhelm J, et al. GLINT: GlucoCEST in neoplastic tumors at 3 T-clinical results of GlucoCEST in gliomas. MAGMA. 2022;35(1):77-85.

137. Hessov I, Bojsen-Møller M, Melsen F. Experimental infusion thrombophlebitis. A comparison between glucose and frutcose and 5% and 10% glucose solution. Intensive Care Med. 1979;5(2):79-81.

138. Puri BK, Lewis HJ, Saeed N, Davey NJ. Volumetric change of the lateral ventricles in the human brain following glucose loading. Exp Physiol. 1999(84):223-6.

139. Nigrovic LE, Kimia AA, Shah SS, Neuman MI. Relationship between cerebrospinal fluid glucose and serum glucose. N Engl J Med. 2012;366(6):576–8.

140. Barnes SL, Whisenant JG, Loveless ME, Yankeelov TE. Practical dynamic contrast enhanced MRI in small animal models of cancer: data acquisition, data analysis, and interpretation. Pharmaceutics. 2012;4(3):442-78.

141. Lavini C, Buiter MS, Maas M. Use of dynamic contrast enhanced time intensity curve shape analysis in MRI: theory and practice. Rep Medical Imaging. 2013(6):71-82.

142. Yabuuchi H, Matsuo Y, Okafuji T, Kamitani T, Soeda H, Setoguchi T, et al. Enhanced mass on contrast-enhanced breast MR imaging: Lesion characterization using combination of dynamic contrast-enhanced and diffusion-weighted MR images. J Magn Reson Imaging. 2008;28(5):1157-65.

143. Lee SH, Kim JH, Park JS, Chang JM, Park SJ, Jung YS, et al. Texture analysis of lesion perfusion volumes in dynamic contrast-enhanced breast MRI. 2008 5th IEEE International Symposium on Biomedical Imaging: From Nano to Macro. 2008:1545-8.

144. Fabijanska A. A novel approach for quantification of time-intensity curves in a DCE-MRI image series with an application to prostate cancer. Comput Biol Med. 2016;73:119-30.

145. Lavini C, Verhoeff JJ, Majoie CB, Stalpers LJ, Richel DJ, Maas M. Model-based, semiquantitative and time intensity curve shape analysis of dynamic contrast-enhanced MRI: a comparison in patients undergoing antiangiogenic treatment for recurrent glioma. J Magn Reson Imaging. 2011;34(6):1303-12.

146. Lavini C, de Jonge MC, van de Sande MG, Tak PP, Nederveen AJ, Maas M. Pixel-by-pixel analysis of DCE MRI curve patterns and an illustration of its application to the imaging of the musculoskeletal system. Magn Reson Imaging. 2007;25(5):604-12.

147. Khalifa F, Soliman A, El-Baz A, Abou El-Ghar M, El-Diasty T, Gimel'farb G, et al. Models and methods for analyzing DCE-MRI: a review. Med Phys. 2014;41(12):124301.

148. Crone C. Facilitated transfer of glucose from blood into brain tissue. J Physiol. 1965;181(1):103-13.

149. Michaelis L, Menten ML. Die Kinetik der Invertinwirkung (The kinetics of invertase action). Biochem Z. 1913;49:333-69.

150. Lund-Andersen H. Transport of glucose from blood to brain. Physiol Rev. 1979;59(2):305-52.

151. Shestov AA, Emir UE, Kumar A, Henry PG, Seaquist ER, Oz G. Simultaneous measurement of glucose transport and utilization in the human brain. Am J Physiol Endocrinol Metab. 2011;301(5):E1040-9.

152. Dienel GA. Chapter 3 - Energy metabolism in the brain. In: Byrne JH, Heidelberger R, Waxham MN, editors. From molecules to networks. 3rd ed: Academic Press; 2014. p. 53-117.

153. Wilson JE. Isozymes of mammalian hexokinase: structure, subcellular localization and metabolic function. J Exp Biol. 2003;206(Pt 12):2049-57.

154. Gruetter R, Ugurbil K, Seaquist ER. Steady-state cerebral glucose concentrations and transport in the human brain. J Neurochem. 1998;70(1):397-408.

155. Crane PD, Pardridge WM, Braun LD, Oldendorf WH. Kinetics of transport and phosphorylation of 2-fluoro-2-deoxy-D-glucose in rat brain. J Neurochem. 1983;40(1):160-7.

156. Gjedde A. High- and low-affinity transport of D-glucose from blood to brain. J Neurochem. 1981;36(4):1463-71.

157. Wienhard K, Pawlik G, Herholz K, Wagner R, Heiss W-D. Estimation of local cerebral glucose utilization by positron emission tomography of [$^{18}$F]2-Fluoro-2-deoxy-D-glucose: a critical appraisal of optimization procedures. J Cereb Blood Flow Metab. 1985;5(1):115-25.

158. Dickie BR, Jin T, Wang P, Hinz R, Harris W, Boutin H, et al. Quantitative kinetic modelling and mapping of cerebral glucose transport and metabolism using glucoCESL MRI. J Cereb Blood Flow Metab. 2022;42(11):2066-79.

159. Cunningham. VJ, Hargreaves. RJ, Pelling. D, Moorhouse. SR. Regional blood-brain glucose transfer in the rat: A novel double-membrane kinetic analysis. J Cereb Blood Flow Metab. 1986;6(3):305-14.

LUND
UNIVERSITY